

Article

Numerical Study of Flow and Particle Deposition in Wall-Flow Filters with Intact or Damaged Exit

Chris D. Dritselis *, Fotini Tzorbatzoglou, Marios Mastrokalos and Onoufrios Haralampous

University of Thessaly, Geopolis, 41500 Larissa, Greece; fotinitzo@uth.gr (F.T.); mmastrok@hotmail.com (M.M.); onoufrios@uth.gr (O.H.)

* Correspondence: dritseli@mie.uth.gr; Tel.: +30-24210-74333

Received: 8 November 2019; Accepted: 25 November 2019; Published: 2 December 2019



Abstract: We examine the time-dependent three-dimensional gas-particle flow in an intact wall-flow filter consisting of channels alternatively plugged at each end and a partially damaged filter in which the rear plugs are removed. Our focus is placed on highlighting the differences in the flow pattern and the deposition process between the two geometries. The Navier–Stokes equations are solved for the fluid flow coupled with a Brinkman/Forchheimer model in order to simulate the flow in the porous walls and plugs. Discrete particle simulation is utilized to determine the nanoparticle trajectories. Using this scheme, we are able to characterize the main features of the flow fields developing in the intact and damaged filters with respect to the Reynolds number and identify those affecting the transport and deposition of particles that have three representative response times. We present fluid velocity iso-contours, which describe the flow regimes inside the channels, as well as in regions upstream and downstream of them. We provide evidence of local recirculating bubbles at the entrance of the channels and after their exit, whereas back-flow occurs in front of the rear plugs of the intact channels. We show that the flow leaves the channels as strong jets that may break up for certain flow parameters, leading to turbulence with features that depend on the presence of the rear plugs. The removal of the rear plugs affects the flow distribution, which, in turn influences the flow rates along the channels and through the walls. We describe the particle trajectories and the topology of deposited particles and show that particles follow closely the streamlines, which may cross the surface of permeable walls for both flow configurations. The distribution of deposited particles resembles the spatial variation of the through-wall flow rate, exhibiting two peak values at both ends of the intact filter channel, and one local maximum near the entrance of the damaged filter channel that is diminished at the exit. We also investigate in detail the particle deposition on the frontal face and indicate that particle accumulation at the edges of the entrance is favored for particles with low response times in flows with high fluid mass rates for both intact and damaged filters. Finally, we examine the filtration efficiency for the defective channels without rear plugs and show that fewer particles are captured as the Reynolds number is increased. A smaller reduction of the filtration efficiency is also predicted with increasing particle size.

Keywords: particulate filter; deposition; numerical simulation; Lagrangian particle tracking; porous media

1. Introduction

It is well-known that diesel engines are responsible for the production of a significant amount of nanoparticles in the urban environment with a profound effect on the human health. Among other filtering techniques, the wall-flow ceramic filter—also known as the diesel particulate filter (DPF)—is the most commonly used technology to control and reduce particulate matter (PM) emissions. More recently, the same technology has been adapted to control PM emissions from gasoline engines.

The strict requirements of the recent legislation call for further development of the particulate filter (PF) technology in synergy with on-board emission control systems. During harsh regeneration, the PF might suffer substrate crack or melting events, resulting in significant particulate matter leakage. In such circumstances, it is also questionable whether the on-board diagnosis (OBD) systems will be capable of responding appropriately, or they will allow the PF failure to go undetected. In this context, an advance of our understanding with respect to the filtration mechanisms in cases of partially damaged PFs is of great importance, which subsequently can facilitate the appraisal of their environmental impact and assist in the design of exhaust systems with effective OBD functionality.

Figure 1a shows the cross-section of a part of a PF and its working principle. The PF consists of several parallel micro-channels of square section, plugged alternatively by ceramic plugs at opposite ends, creating a chessboard pattern. The particle-laden flow is driven into the inlet channels (opened at the entrance), the gas is forced to flow through the permeable ceramic walls into the outlet channels (opened at the exit), while the soot particles deposit in the micro-pores of the walls.

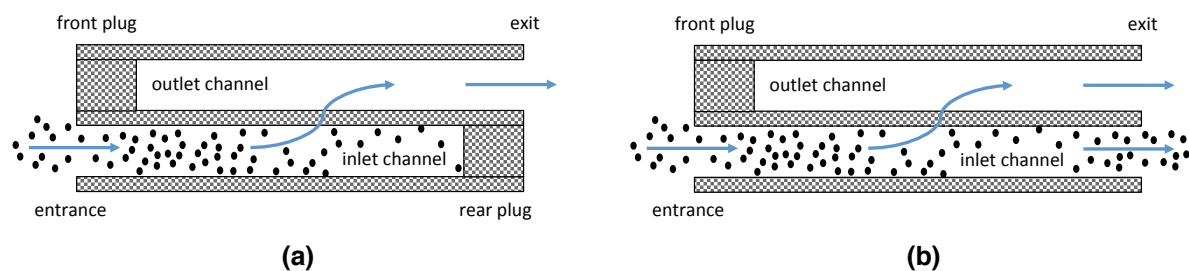


Figure 1. Schematic of wall-flow particulate filters with intact (a) or damaged exit (b) and their working principle.

The PF has been studied for more than three decades. The vast majority of the experiments have been conducted outside of the filter, while numerical modeling has mostly been used to predict the flow and physico-chemical phenomena that take place inside the PF. The very first one-dimensional (1D) model was proposed by Bisset [1]. Most subsequent models have been based on this initial work, while several extensions and/or improvements have been proposed (see, for example, References [2–7]). Model tuning and validation are generally required and this is accomplished through comparisons of the model predictions against macroscopic measurements, such as the pressure drop and inlet/outlet gas temperatures.

There is a small number of numerical studies dealing with the gas-particle flow in the micro-channels of the ceramic filter based on sophisticated three-dimensional (3D) simulations. By using a commercial computational fluid dynamics (CFD) software, Konstandopoulos et al. [8] performed 3D simulations in PFs mainly to calibrate simpler 1D models. Sbrizzai et al. [9] conducted 3D steady-state fluid flow simulations coupled with Lagrangian particle tracking to model the trajectories of non-deformable, non-interacting, solid spheres in the limit of one-way coupling between the fluid and particulate phases. They found that the particles exhibited a greater tendency to deposit at the end of the inlet channels as their size was increased. No particle deposition was observed at the entrance section that was attributed to the flow contraction. Bensaid et al. [10,11] adopted a 3D Eulerian–Eulerian approach to simulate the gas-particle flow in a PF. Predictions of the deposited soot concentration, the filtration efficiency and the temperature were given, aimed to assist the design of the filter trap. Lee and Lee [12] also utilized an Eulerian–Eulerian approach to investigate the two-phase flow in a PF. They showed that more particles were deposited in areas near the entrance and at the end of the inlet channels.

Konstandopoulos et al. [13] and Liu and Miller [14] performed 3D CFD simulations in order to evaluate the effect of the gas flow contraction and expansion at the ends of a filter that is formed of square and triangular channels, respectively. In both studies, the flow at the filter exit consists of high velocity jets and recirculating fluid areas behind the rear plugs. However, in Konstandopoulos et al. [13],

the flow at the entrance was smoothly contracted into the inlet channels and the exiting jets induced strong mixing and pressure fluctuations for several plug lengths downstream of the filter. In contrast, Liu and Miller [14] found recirculations adjacent to the front and rear plugs.

There are also a few works on two-dimensional (2D) models applying a commercial CFD software (see, for example, References [15–17]). It turns out that little improvement is gained by the 2D models when compared with the 1D models, while significant flow detail is lost relative to the 3D models.

Experiments are generally time-consuming and costly, and conducting accurate local measurements inside the filter with good repeatability is a quite challenging task. Recently, the wall-flow in a PF has been analyzed experimentally by Cooper et al. [18]. They measured the fluid velocities and turbulent diffusivity at the entrance and exit of a PF based on gas-phase compressed sensing magnetic resonance methods. They indicated that the velocity at the entrance was smooth and it gradually evolved from a plug to a laminar flow distribution along the length of the inlet channel. At the filter exit, well-defined jets leaving the outlet channels were observed, as well as regions of stagnant and recirculating gas next to the rear plugs. Results of turbulent diffusivity pointed out that fluid turbulence occurred mainly in front of the filter and at its exit. Imaging techniques have also been used previously to conduct indirect measurements of the gas flow in PFs (see, for example, References [19,20]). The primary interest in these works was to demonstrate the feasibility of the experimental method in the case of a PF.

Over the last years, the investigation of partially damaged PFs has received considerable attention. For example, Samaras [21] and Finch et al. [22] showed that monitoring of the back-pressure in failed PFs, in which the rear plugs were removed artificially, is not adequate for on-board diagnostic purpose. There are also some numerical works utilizing 1D models for flawed PFs without rear plugs [23–26]. The above-mentioned studies rely on the initial work of Bisset [1] and incorporate proper model adjustments to account for the missing plugs.

In the literature, there is a lack of detailed CFD simulations of 3D gas-particle flows in defective wall-flow PFs, which motivated our study. The objective of the present work is the investigation of the fluid flow regimes and of the particle deposition in damaged PFs with missing rear plugs (see Figure 1b). The results are compared with those obtained for an intact filter. Several numerical simulations are performed by solving the 3D Navier–Stokes equations for the flow of the carrier phase together with Lagrangian particle tracking for the dispersed phase. The Brinkman model with an additional Forchheimer term has been used to simulate the flow in the porous walls and plugs. To the best knowledge of the authors, this problem has not been addressed previously. The adopted numerical formulation has not been used in the past for the investigation of the time-dependent 3D gas-particle flow in PFs. Moreover, numerical results of particle deposition on the frontal face of the PFs are provided for the first time. Except for their theoretical value, the present results aim at assisting the prediction of flow and filtration phenomena in intact and partially damaged PFs.

2. Governing Equations

2.1. Carrier Phase Flow

Figure 2 shows the computational domain considered in this work, which is the same for both the intact and damaged filters. However, in the latter case, the rear plugs are removed. More specifically, an elementary cell of the filters is examined, consisting of two inlet (dirty) and two outlet (clean) square channels, which forms the overall structures when reproduced periodically in the y and z -directions. The entrance and exit of the domain are located at distances L_u and L_d away from the ends of the filters, respectively, in order to ensure that the fluid flow in the proximity of the elements is not influenced by the numerically imposed boundary conditions. The porous walls and plugs are isotropic, homogeneous and saturated with a single-phase fluid, whereas their porosity ϵ_w and permeability k_w are uniform.

The Navier–Stokes equations are employed to simulate the flow in the clear fluid, while the volume-averaged Navier–Stokes equations based on the Brinkman model with an additional Forchheimer term are utilized in the permeable walls and plugs of the PFs. The velocity averaged over a volume containing only fluid u and the velocity averaged over an elementary volume of solid matrix plus fluid u^* are related to each other by the Dupuit–Forchheimer equation $u = \epsilon u^*$ [27], where ϵ is the porosity. The non-dimensional governing equations written as a single set of equations that are applicable in both the fluid and porous regions are [28–30]:

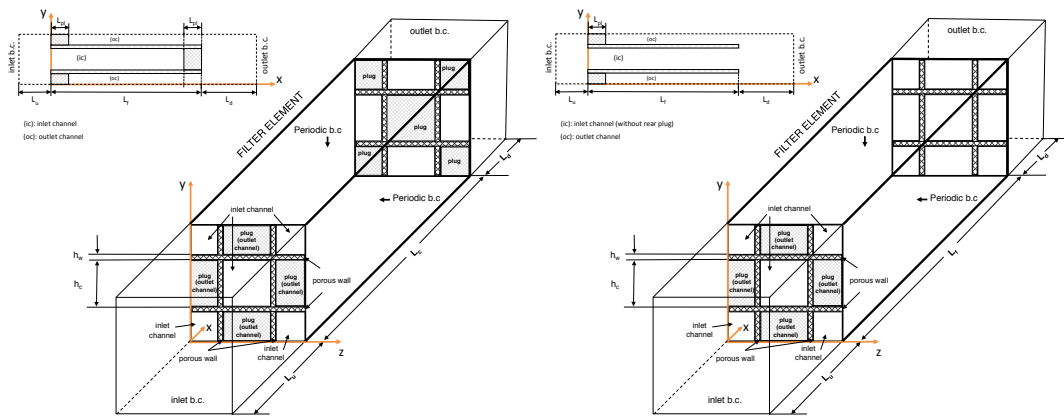


Figure 2. Present geometry and flow configuration for the intact filter (left) and the damaged filter without rear plugs (right).

$$\nabla \cdot \mathbf{U} = 0, \tag{1}$$

$$\frac{\partial \mathbf{U}}{\partial T} + \frac{1}{\epsilon} \mathbf{U} \cdot \nabla \mathbf{U} = -\epsilon \nabla P + \frac{\Lambda}{Re} \nabla^2 \mathbf{U} + \mathbf{F}_{DR}, \tag{2}$$

$$\mathbf{F}_{DR} = -C_1 \frac{\epsilon}{Re Da} \mathbf{U} - C_2 \frac{f \epsilon}{\sqrt{Da}} |\mathbf{U}| \mathbf{U}, \tag{3}$$

where $\mathbf{U} = (U, V, W)/u_0$ is the velocity vector and U, V, W are the velocity components in the $x, y,$ and z -directions, respectively, $P = p/\rho u_0^2$ is the pressure, ρ is the fluid density, and $T = t u_0/h$ is the time. Throughout the paper, vectors are represented by bold fonts, while capital fonts denote non-dimensional quantities. The above equations and all the quantities are made non-dimensional by using the side of the square channels h_c , the inlet velocity in the streamwise direction u_0 , and h_c/u_0 as the characteristic length, velocity, and time scales, respectively. The non-dimensional parameters appearing in Equations (1)–(3) are the Reynolds number $Re = \rho u_0 h_c/\mu$ and the Darcy number $Da = k/h_c^2$, where μ (ν) is the fluid dynamic (kinematic) viscosity and k is the permeability. The vector \mathbf{F}_{DR} is the drag force per unit mass that the solid phase of the porous walls and plugs exerts on the fluid phase. The first term in Equation (3) represents the standard drag force in the limit of Stokes flow in the pores, while the second term corrects the drag force to account for inertial effects at higher Reynolds numbers. C_1, C_2 are binary constants obtaining 0 and 1 outside of the porous regions and inside them, respectively. The porosity ϵ is set to $0 < \epsilon = \epsilon_w < 1$ in the permeable walls and plugs and to unity in the clear fluid region. $\Lambda = \mu_e/\mu = 1$ is the ratio between the dynamic viscosity in the porous (μ_e) and fluid (μ) regions. The Forchheimer coefficient f can be calculated depending on the micro-structure of the porous medium. In this work, the Ergun correlation is used that is expressed as [27]:

$$f = \frac{1.75}{\sqrt{150\epsilon^3}}. \tag{4}$$

The calculation of permeability k can be related to the porosity ϵ by using the following expression (see, for example, Reference [29]):

$$k = \frac{\Phi_s}{180} \frac{\epsilon^3 d_{p,ob}^2}{(1 - \epsilon)^2}, \tag{5}$$

where $d_{p,ob} = 6V_{p,ob} / A_{p,ob}$ is the average obstacle size of the porous region, $V_{p,ob}$ and $A_{p,ob}$ denote the volume and the surface of the solid obstacles, respectively, and Φ_s is the sphericity of the obstacles. The linear and non-linear parts of the drag force \mathbf{F}_{DR} may be re-arranged as follows:

$$\mathbf{F}_{DR} = -C_1 \frac{\epsilon}{Re Da} \mathbf{U} - C_2 \frac{f \epsilon}{Re Da} |\mathbf{U}| \mathbf{U}, \tag{6}$$

where the coefficient f is now given as $f = \Phi_s \tilde{f} u_0$, and \tilde{f} is expressed as [29]:

$$\tilde{f} = \frac{\epsilon}{100(1 - \epsilon)} \frac{d_{p,ob}}{\nu}. \tag{7}$$

There are no solid obstructions in the clear fluid and, thus, ϵ is set to unity, the drag force terms are vanished, and the governing equations reduce to the standard Navier–Stokes equations. In this case, the velocity \mathbf{U} corresponds to the fluid velocity \mathbf{U}^f that is obtained by the numerical solution of the Navier–Stokes equations in the fluid region and it holds that $\mathbf{U} = \mathbf{U}^* = \mathbf{U}^f$.

Appropriate boundary conditions are applied to the domain boundaries. Inlet conditions $U = 1$, $V = W = 0$ are placed upstream of the front face of the filters. It should be noted that the inlet flow in a PF is rather turbulent and/or pulsating. However, the present work deals only with constant flows at the inlet, partly because there is lack of precise and reliable information regarding the frequency and amplitude of the fluid velocity fluctuations in front of the PFs. But more importantly, the above inlet boundary conditions are usually used in the majority of the past numerical studies (see, for example, References [9–12]) or they are suggested by recent experiments [18] and, thus, their adoption allows comparisons of the present results against previous findings at least from a qualitative point of view. Convective boundary conditions [31] are used downstream of the exit of the filters expressed as:

$$\frac{\partial \phi}{\partial T} + U_{c,av} \frac{\partial \phi}{\partial X} = 0, \tag{8}$$

where $U_{c,av} = 1$ is the average non-dimensional velocity in the streamwise x -direction, and ϕ is U , V , or W . These boundary conditions are appropriate for the flow under investigation, and they ensure that large-scale vortices and jet-like structures can pass the outflow boundary without producing significant disturbances or reflections into the internal flow domain. Periodic boundary conditions are applied to all boundaries normal to the y and z -directions.

In the case of a composite system consisting of a fluid and porous medium, it is necessary to solve simultaneously the Navier–Stokes equations in the fluid region and the Brinkman equations in the porous region together with proper matching conditions at the interfaces. As seen above, the two sets of governing equations for the fluid and porous regions are combined into one set of conservation equations by introducing binary parameters. Such single-domain approach has been used extensively in the past [28,30,32–34]. Although this method is relatively easier to implement numerically, special care must be taken into account to simulate correctly the flow adjacent to the interfaces. The harmonic-mean formulation suggested by Patankar [35] is usually adopted in order to handle the abrupt change in the porosity and permeability at the interface. Here, the following conditions that are proper for the description of the flow at the fluid/porous interface are explicitly applied [36,37]:

$$\mathbf{U}_{\perp}^f = \mathbf{U}_{\perp}^w, \tag{9}$$

$$\mathbf{U}_{\parallel}^f = \mathbf{U}_{\parallel}^w, \tag{10}$$

$$P^f = \frac{1}{\epsilon} P^w, \tag{11}$$

$$\frac{\partial \mathbf{U}_{\perp}^f}{\partial n} - \frac{1}{\epsilon} \frac{\partial \mathbf{U}_{\perp}^w}{\partial n} = 0, \tag{12}$$

where the symbols \perp and \parallel indicate velocity components that are perpendicular and parallel to the interface, respectively, the superscripts f and w denote quantities in the fluid and porous walls and plugs, respectively, and n is the unit vector normal to the interface. Note that the derivatives of the velocity components \mathbf{U}_{\perp}^f in Equation (12) are taken within the fluid region, while those of the \mathbf{U}_{\parallel}^w velocity components are taken within the porous walls and plugs. The implementation of Equations (9) to (12) requires a relatively small number of code adjustments in the grid points adjacent to the interfaces, allowing the numerical solution of the present conjugate problem in the whole domain (fluid and porous regions) based on CFD methods that have been developed initially to deal fluid flows.

2.2. Dispersed Particulate Phase

Once a fully developed flow in the PFs is numerically obtained, the fluid velocity field is used to study the transport and deposition of the particulate phase. For particles having size smaller than the mean free path of the molecules of the carrier gas, the fluid around them cannot be considered a continuum. The particles are affected by collisions with individual molecules, and at times they slip between the molecules. Thus, two main effects are introduced when considering sub-micron particles [9,38,39]—(a) a reduction to the drag coefficient due to the slip, and (b) a Brownian force that modifies randomly the particle trajectory. In the present work, the dominant forces acting on a particle are the drag and Brownian forces. More specifically, the particle trajectory is determined in a Lagrangian reference frame based on the following non-dimensional equation of motion [40]:

$$\frac{d\mathbf{U}_p}{dT} = -\frac{3}{2C_c(2S+1)} \frac{C_D}{D_p} |\mathbf{U}_p - \mathbf{U}(\mathbf{X}_p)| (\mathbf{U}_p - \mathbf{U}(\mathbf{X}_p)) + \mathbf{N}(T), \tag{13}$$

where $\mathbf{U}_p = d\mathbf{X}_p/dT$ is the particle velocity vector, $\mathbf{U}(\mathbf{X}_p)$ is the fluid velocity vector calculated at the particle position \mathbf{X}_p , S is the ratio between the particle density ρ_p and the fluid density ρ , and $D_p (= d_p/h_c)$ is the particle diameter. The first and second terms of the right-hand side of Equation (13) are the drag and Brownian forces per particle mass, respectively. The quantity C_c is the Stokes–Cunningham slip correction coefficient calculated as [40]:

$$C_c = 1 + 2Kn [1.257 + 0.4 \exp(-0.55 Kn)]. \tag{14}$$

The parameter Kn is the Knudsen number defined as the ratio of the mean free path of gas molecules λ and the particle diameter d_p :

$$Kn = \frac{\lambda}{d_p}. \tag{15}$$

The coefficient C_D corrects the drag force for inertial effects at non-negligible values of the particle Reynolds number, $Re_p = |\mathbf{u}_p - \mathbf{u}| d_p/\nu = |\mathbf{U}_p - \mathbf{U}| D_p Re$, and it is given as [41]:

$$C_D = \frac{24}{Re_p} \left(1 + 0.15 Re_p^{0.687}\right). \tag{16}$$

The Brownian force per particle mass $\mathbf{N}(T)$ is modeled as Gaussian white noise random process [39,40]. The i -component of the non-dimensional Brownian force is evaluated at every time step of the simulations as:

$$N_i = G_i \sqrt{\frac{2}{Sc T_p^2 Re \Delta T}}, \tag{17}$$

where G_i is zero mean, unit variance independent Gaussian random number, ΔT is the time step used in the simulations, $T_p = C_c S D_p^2 / 18 Re$ is the non-dimensional particle response time, and Sc is the Schmidt number calculated as:

$$Sc = \frac{\nu}{\alpha_B} = \frac{3\nu \pi \mu d_p}{k_B \theta C_c}. \quad (18)$$

Here, α_B is the Brownian diffusivity, θ is the absolute temperature, and $k_B = 1.32 \times 10^{-23} \text{ J K}^{-1}$ is the Boltzmann constant. The quantity G_i is computed by using the Muller-box method from two randomly chosen numbers r_1 and r_2 selected from a uniform distribution [39]:

$$G_i = \sqrt{-2 \ln r_1} \cos(2\pi r_2). \quad (19)$$

Dilute flow conditions are assumed and, thus, the fluid flow under investigation is not influenced by the momentum exchange with the particulate phase, neither particle-particle interactions are taken into account. This assumption is fully justified in cases with particles having very low response times at low total mass and volume fractions (see, for example, Reference [42] and references therein). In the context of PFs, this choice is logical given the fact that the Stokes number of the particles is very small (for example, it is of the order of $O(10^{-3})$ to $O(10^{-6})$ in the present work), which results in negligible slip velocities between the two phases, while the concentration of soot particles is generally low at early filtration stages (see References [9–11]). Initially, the particles are uniformly distributed at the inlet plane with velocities equal to those of the fluid at their positions. The particles exiting the computational domain through the planes normal to the periodic y, z -directions are re-introduced in it from the corresponding opposite boundary plane with their exiting velocities. Perfectly absorbing walls and plugs (see, for example, Reference [9]) are considered and, thus, the particles are assumed to deposit when their center is less than $D_p/2$ distance from the surfaces of the porous regions.

3. Numerical Methods and Details

3.1. Overview of the Simulations

The particulate traps under investigation are those studied experimentally in Haralampous et al. [43]. The side of each square channel is $h_c = 1.2 \text{ mm}$, the thickness of the porous walls is $h_w = 0.3 \text{ mm}$, while their dimensionless values are $H_c = 1$ and $H_w = 0.25$, respectively. The streamwise extent of the front and rear porous plugs is $L_{pl} = 4.2$, and the length of the filters is $L_f = 127$ ($l_f = 152,4 \text{ mm}$). The entrance of the filters in the x -direction is placed at $X = 0$. The inlet and outlet boundaries are located at distances $L_u = 15$ and $L_d = 28$ upstream and downstream of the elements, respectively. The size of the computational domain is $L_x = 170$ in the streamwise x -direction and $L_y = L_z = 2.5$ in the periodic y, z -directions.

The temperature is $\theta_0 = 540 \text{ K}$ throughout the domain, the fluid density is $\rho = 0.6509 \text{ kg m}^{-3}$, and its dynamic (kinematic) viscosity is $\mu = 2.54 \times 10^{-5} \text{ kg m}^{-1} \text{ s}^{-1}$ ($\nu = 3.91 \times 10^{-5} \text{ m}^2 \text{ s}^{-1}$). The values of the Reynolds number examined here are $Re_0 = u_0 h_c / \nu = 65, 163, 261, \text{ and } 522$ that correspond to mass flow rates of $\dot{m} = 0.623, 1.246, 2.492, \text{ and } 4.984 \text{ kg s}^{-1} (\times 10^5)$ and inlet fluid velocities of $u_0 = 6.65, 13.3, 26.6, \text{ and } 53.2 \text{ m s}^{-1}$. The values of the Reynolds number based on the bulk velocity at the entrance of the inlet channels are $Re_c = u_c h_c / \nu = 204, 408, 629, 816, \text{ and } 1632$. The porosity of the walls and plugs is $\epsilon_w = 0.52$ and their permeability is $k_w = 6.18 \times 10^{-13} \text{ m}^2$, while the average size of obstacles in the porous domain is $d_{p,ob} = 27.7 \text{ }\mu\text{m}$. These values correspond to the clean wall case examined experimentally in [43]. The results shown here were obtained based on Equations (5) to (7) in order to model F_{DR} , while Equations (3) and (4) were used in the verification tests. It was confirmed that the non-linear corrections to the drag force are negligible for the problem under investigation and, thus, Equations (3) and (6) reduce to the same expression and produce the same results. The sphericity Φ_s was given a suitable value so that the permeability yielded by Equation (5) matched k_w .

An explicit fractional step method is used to solve numerically the governing fluid flow equations on a staggered mesh. All spatial derivatives are approximated by second-order central finite differences. The equations are advanced in time with a pressure-correction method. The time discretization is based on an explicit low-storage third-order Runge–Kutta scheme. Details about the numerical schemes can be found in Dritselis and Vlachos [42]. The results shown in the present work were obtained by using $436 \times 121 \times 121$. The mesh in the x -direction is refined in the front and rear faces of the plugs. The distance of the first grid point outside of the porous domain is $\Delta X_{min} = 0.004$. The maximum grid spacing upstream and downstream of the filters is $\Delta X_{max} = 1.5$ and 0.5 , respectively, while it is $\Delta X_{max} = 4$ inside the channels. The spacing of the uniform computational mesh in the periodic y and z -directions is $\Delta Y = \Delta Z = 0.02$.

The transport and deposition of the dispersed phase is studied for three ensembles of particles having diameter $d_p = 20, 60, \text{ and } 200 \text{ nm}$ and density $\rho_p = 1409, 762, \text{ and } 388 \text{ kg m}^{-3}$, respectively. This, the mean free path is estimated as $\lambda = 1.225 \times 10^{-7} \text{ m}$ using the Equations of Sharipov and Seleznev [44]. The values of the Knudsen number are $Kn = 6.127, 2.042, \text{ and } 0.613$ for the three particle sets. It can be seen that the values of the Knudsen number are within the transitional flow regime for $0.25 < Kn < 10$ [38]. Results for the particulate phase are obtained by following the trajectories of 10^5 particles.

The positions and velocities of the particles are calculated based on an explicit second-order Adams–Bashforth method. The fluid velocity at the particle position is obtained by tri-linear interpolation between the particle position and the nearby grid points. Particle deposition is detected as geometric intersection of the particle trajectory and the walls or plugs. The detection algorithm of particle deposition is similar to that used in our previous work [45]. The reader is referred to Dritselis [46] for more details on the numerical schemes regarding the Lagrangian particle tracking.

3.2. Grid Independence Tests

A grid sensitivity analysis was conducted to ensure that the results shown in the present work are grid converged. Figure 3a,b show representative results for the time history of the center-line streamwise velocity at the inlet channel entrance and at the outlet channel exit, respectively, for an extreme grid-demanding case of $Re_c = 1632$. Six computational meshes $332 \times 81 \times 81, 436 \times 81 \times 81, 752 \times 81 \times 81, 436 \times 101 \times 101, 436 \times 121 \times 121, \text{ and } 436 \times 151 \times 151$ were examined. Figure 3 indicates that the results are converged with grid refinement. More specifically, the instantaneous velocity at the entrance of the filter is gradually increased and it obtains a constant value at times $T > 1$ as shown in Figure 3a. A maximum difference of about 0.92% is observed by using 752 ($U = 2.921$) grid points in the x -direction as compared with the case of 436 ($U = 2.894$) grid points. For the computational meshes with 436 grid points in the x -direction, the values of U at time $T = 5$ are 2.894, 2.948, 2.987 and 3.011 for 81, 101, 121 and 151 grid points in the y, z directions, respectively. It can be seen that when utilizing 121 grid points in the periodic directions, a maximum difference of 0.8% is found relative to the next finer computational mesh. At the exit of the filter, the flow exhibits clearly turbulent fluctuations, and the time evolution of U differs between the various meshes. However, the time-averaged velocity converges with grid refinement, similarly to what is found for the instantaneous U at the entrance of the inlet channel. For example, the values of the time-averaged U velocity for the distributions shown in Figure 3b are 5.439, 5.505, and 5.559 for 101, 121, and 151 grid points in the y, z -directions, respectively. As the mesh is refined from 121 to 151 grid points, differences smaller than 0.96% are obtained. Thus, it can be concluded that grid independence of the results is achieved when choosing a computational mesh consisting of $436 \times 121 \times 121$ grid points. The presently adopted grid resolution is capable of resolving adequately the most significant flow scales, and its use can yield accurate results that describe the laminar and turbulent flow regimes in a PF element for the range of parameters examined here. Similar observations can be made when examining other flow quantities, such as the V, W velocity components, and the pressure P at several locations in the computational domain.

Grid independence tests were also performed in the case of damaged filter without rear plugs, which confirmed the adequacy of the finally chosen computational mesh.

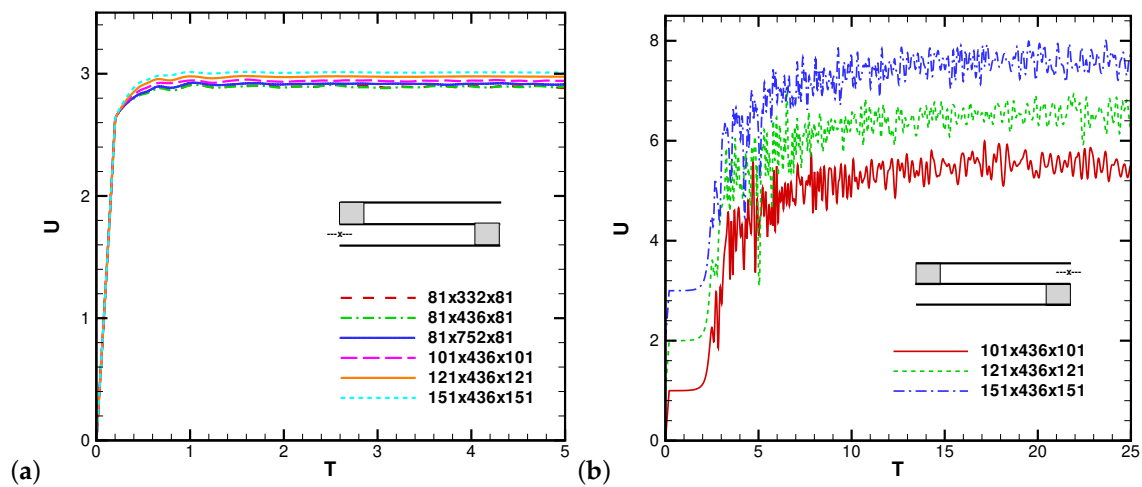


Figure 3. Time evolution of the center-line streamwise fluid velocity U at the entrance (a) and exit (b) of the intact filter element for several computational meshes at $Re_c = 1632$. In (b), the U values for the meshes $121 \times 436 \times 121$ and $151 \times 436 \times 151$ are shifted upwards by 1.5 and 3, respectively.

4. Verification

The accuracy of our numerical code to predict several fluid flows has been demonstrated in previous works [42,45]. Similarly, the accuracy of the Lagrangian particle tracking to simulate the transport of particles and their deposition has also been successfully verified in certain cases [45,46]. The present numerical treatment of the porous media is verified in three test cases—(a) the fully developed flow in a channel partially filled with a layer of a porous medium (Beavers–Joseph flow problem), (b) the flow through a channel with a porous plug, and (c) the flow around a square porous cylinder. The successful verification, as it will be seen in the next subsections, proves that the adopted formulation (Equations (1) to (12), the numerical algorithm chosen for the spatial and time discretization of these equations and their solution) has the potential to reproduce accurate and reliable results for flows over homogeneous porous media.

4.1. Flow in a Channel Partially Filled with a Layer of a Porous Medium (Beavers–Joseph Flow Problem)

The first verification test conducted corresponds to the Beavers–Joseph flow problem (for more details about the problem formulation, please see References [47,48]). The physical domain consists of a parallel-plate channel, which is horizontally divided into a fluid region with height h_1 above and a homogeneous porous region saturated by fluid with height h_2 below. Here, the case $h_2 = h_1 = h = 1$ is examined. A 2D computational domain of $2h \times 2h$ is used that is discretized by a mesh of 41×41 grid points. Periodic boundary conditions are applied in the x -direction and no-slip conditions are enforced at the walls in the y -direction. A uniform pressure gradient is imposed in the streamwise direction that results in a fully developed flow at $Re = u_0 h / \nu = 1$. Figure 4 shows the $U (= u / u_0)$ velocity profile for two representative cases at $Da = 10^{-2}, 10^{-3}$, and $\epsilon = 0.7$. A comparison of the present predictions against those of Costa et al. [47] is also shown, indicating a good agreement of the results between the studies.

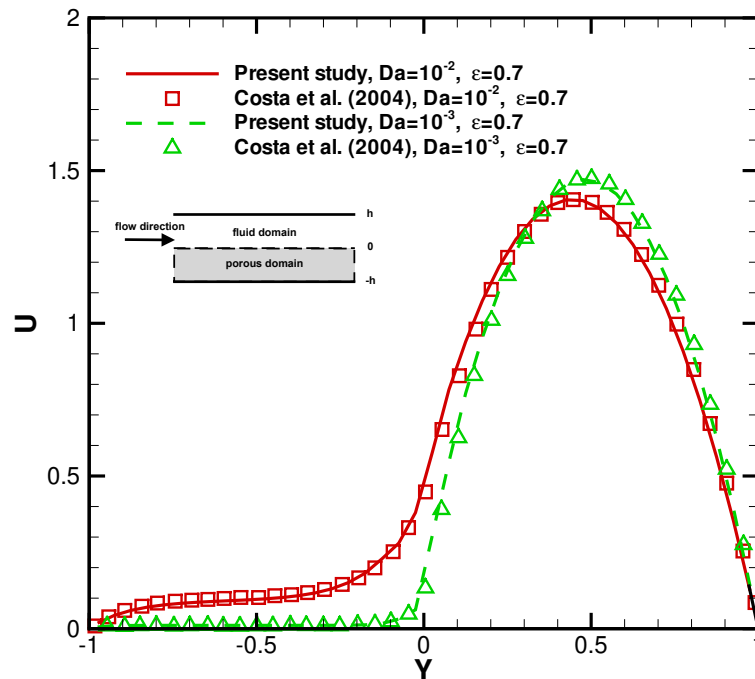


Figure 4. Distribution of the non-dimensional streamwise velocity component U with the wall-normal distance Y for $Re = 1$, $\epsilon = 0.7$, and $Da = 10^{-2}, 10^{-3}$. Lines: present results; symbols: results of Costa et al. [47].

4.2. Flow through a Channel with a Porous Plug

In this test problem, the flow passes through a 2D channel with a porous plug under an imposed overall pressure gradient. Away from the plug, there are two fluid regions where the flow is fully developed. The streamwise extent of the plug is $2h$, while each one of the two fluid regions have size $3h$. The distance between the walls of the channel is h and, thus, the total computational domain is $(3h + 2h + 3h) \times h$. The computational mesh consists of $(21 + 21 + 21) \times 21$ grid points that are unevenly distributed in the x -direction, so that the grid spacing is thinner near the interfaces, and uniformly in the y -direction. Periodic boundary conditions are applied at distances $3h$ upstream and downstream of the plug, while a global non-dimensional pressure difference is imposed in order to give rise a flow having $Re = u_0 h / \nu = 1$. No-slip conditions are applied at the channel walls. Further details about the problem setup can be found in References [47,48]. Figure 5 shows the center-line velocity $U (= u/u_0)$ and pressure $P (= p/\rho u_0^2)$ along the x -direction at $Da = 10^{-2}$ and $\epsilon = 0.7$. A rapid reduction of the velocity is observed in the plug, accompanied by a large pressure drop. In accordance with previous findings [47,48], an essentially 1D flow is found over most of the fluid and porous regions, with the exception of the vicinity of the fluid/plug interfaces, where the flow is predominantly 2D. It can be seen that the present results are in good agreement with those of Costa et al. [47] in the case of continuous stress conditions at the interfaces between the fluid and the porous medium.

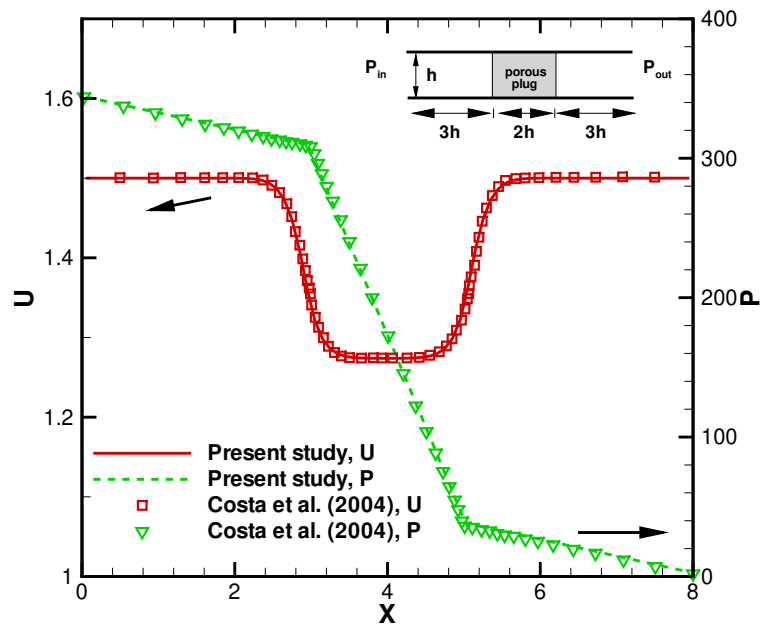


Figure 5. Variation of the center-line velocity component U and pressure P in the streamwise x -direction for $Re = 1$, $\epsilon = 0.7$, and $Da = 10^{-2}, 10^{-3}$. Lines: present results; symbols: results of Costa et al. [47].

4.3. Flow around a Square Porous Cylinder

The geometric configuration of the last verification test is shown in Figure 6a. A fixed 2D square porous cylinder with sides of length $h = 1$ is exposed to a constant free-stream velocity. The size of the computational domain is $25h \times 25h$ in the x -direction (flow direction) and y -direction, respectively. The top and bottom boundaries of the calculation domain are free-slip. Inflow boundary conditions are prescribed at the left ($U = u/u_0 = 1, V = 0$), while convective boundary conditions are applied at the right with an average non-dimensional convective velocity equal to unity. The reader may refer to Dhinakaran and Ponmozhi [34] for additional details regarding the problem formulation. A non-uniform grid distribution is used consisting of 111×111 grid points in the x, y -directions, respectively. The grid is stretched so that the minimum distance of the first grid point from the fluid/porous interface is $0.001 h$, while the grid size away from the square cylinder is approximately $0.2 h$. At first, it was confirmed that the results of the flow around an impermeable, solid square cylinder in an unbounded domain are reproduced when setting the Darcy number and the porosity to very low values. Figure 6b shows the drag coefficient C_D as a function of the Reynolds number ($5 \leq Re = u_0 h/\nu \leq 40$) in the case of a permeable square cylinder at $Da = 10^{-4}$ and $\epsilon = 0.8$. It can be seen that the present results agree reasonably well with those obtained by Dhinakaran and Ponmozhi [34]. Figure 6b also shows that even the use of a uniform mesh of 251×251 grid points can yield adequately the variation of the drag coefficient, especially as the Reynolds number increases.

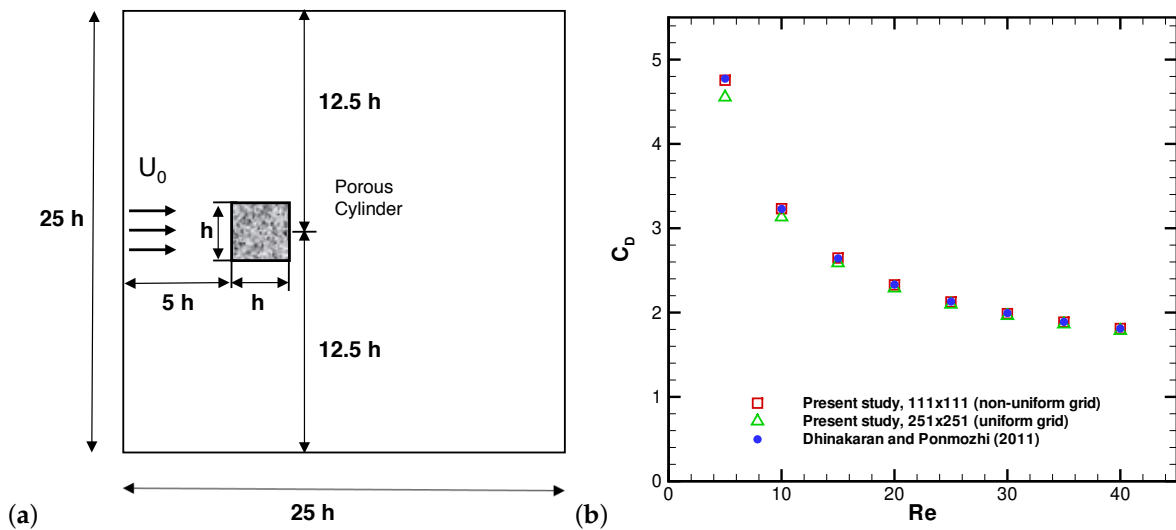


Figure 6. (a) The geometric configuration for the unconfined flow around a permeable square cylinder, (b) the drag coefficient C_D as a function of the Reynolds number at $Da = 10^{-4}$ and $\epsilon = 0.8$. Open symbols: present results; closed symbols: results of Dhinakaran and Ponmozhi [34].

5. Results and Discussion

In this section, representative results are presented in order to highlight the main features of the fluid flow in filters with intact or damaged exit and their differences and assess their impact on the particle deposition process.

5.1. Fluid Velocity and Pressure Fields

Figure 7a shows the instantaneous U velocity component of the carrier phase in y - z planes placed at different distances along the x -direction for a representative case of intact filter at $Re_c = 1632$. These planes are indicated in the insert above the figure by the dotted lines against the filter element. The fluid flow is almost uniform upstream of the channels (plane A). As the entrance of the inlet channels is approached, the flow is contracted (plane B), obtaining a velocity distribution that corresponds to a plug flow (plane C). The fluid flow is gradually developed into a parabolic profile (planes D and E). A symmetric velocity distribution is apparent, exhibiting a maximum value at the center of the inlet channels. It is found that the center-line U velocity is increased up to 30% of the channel length (planes C–D) and it is then decreased with further increasing distance from the entrance (planes E, F and G). A back-flow can be seen, indicated by blue color, which becomes considerable and covers a significant portion of plane F. The spatial evolution of the U velocity inside the outlet channels is nearly complementary to that described above for the inlet channels (planes C–G). For example, the velocity is adjusted to a laminar parabolic distribution as proceeding in the streamwise direction. In contrast to the inlet channels, the center-line U velocity is now increased monotonously. As expected, the fluid flow leaves the outlet channels as strong jet-like events. The jets are accompanied by large recirculation areas located in the wake of the rear plugs (planes H–J). The red regions correspond to the jets and the blue regions indicate negative values of the U velocity. A non-homogeneous turbulent field is obtained and maintained at a sufficient distance downstream of the intact filter element (plane K). However, it becomes weaker and relatively homogeneous farther away from it (plane L).

Figure 7b shows the development of the U velocity in the x -direction for the damaged filter without rear plugs at $Re_c = 1632$. The flow evolution in front of the defective filter element, as well as in the first part of the channels resembles that of the intact filter (planes A, B, C, D and E). Most of the fluid flow escapes now from the unplugged inlet channels (planes F and G) and, thus, a smaller amount of fluid passes through the permeable walls into the outlet channels. Lower U velocities are generally found at the exit of the damaged filter relative to the intact filter. In the region after the defective

element, there are four fluid jets together with small recirculating regions having sizes of the order of the permeable wall thickness (planes H, I, J, and K). The jets arising out of the unplugged inlet channels are stronger than those exiting from the outlet channels, while they are both weaker as compared with the jets appearing in the intact filter element. Further away from the exit, an inhomogeneous, non-sustainable turbulence becomes visible (plane L). It is noted that the characteristics of the fluid turbulence are generally different between the two flow configurations.

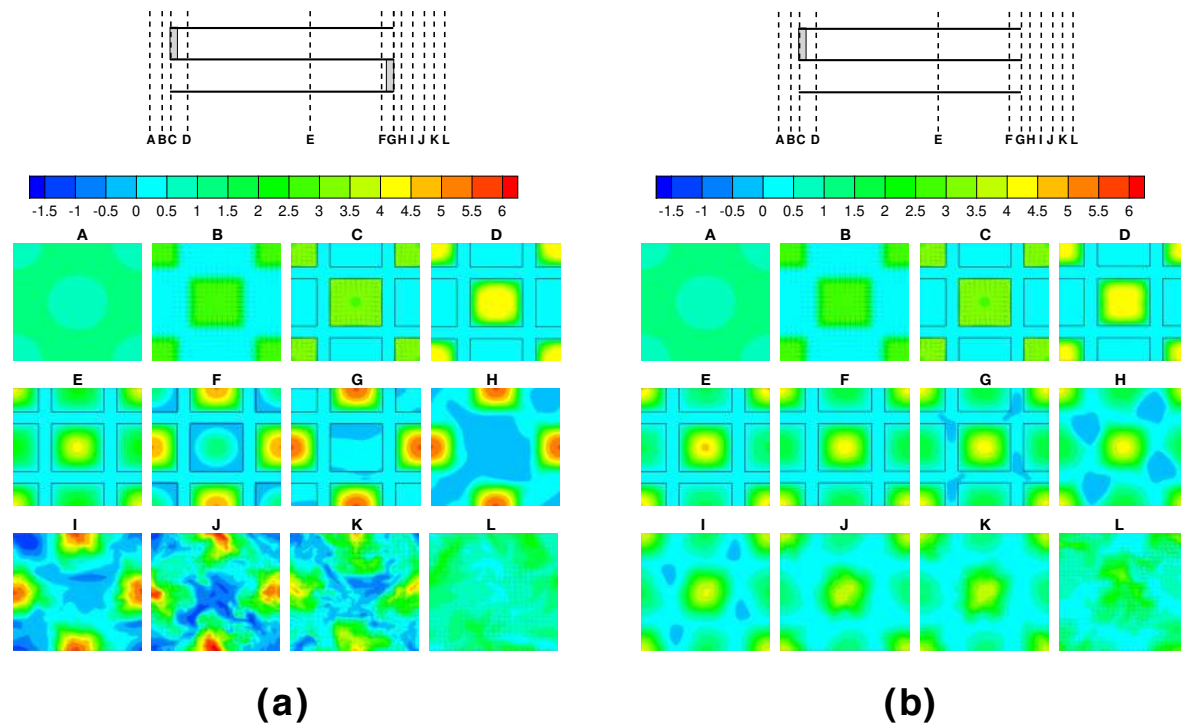


Figure 7. Evolution in the x -direction of the U velocity for the intact (a) and damaged (b) filters at $Re_c = 1632$. The y - z planes A, B, C, D, E, F, G, H, I, J, K, and L correspond to $X = -10.02$ (A), -0.59 (B), 0 (C), 10.27 (D), 79.54 (E), 120.11 (F), 126.98 (G), 128.08 (H), 132.32 (I), 135.10 (J), 140.37 (K), and 146.06 (L), respectively.

The flow fields of the carrier phase in the intact and damaged filters at different Reynolds numbers are similar to those presented for $Re_c = 1632$. However, there are some key differences that can be noticed in the inlet, exit and downstream of the elements at small Re_c values. More specifically, Figure 8a,b show the streamlines near the entrance of the intact filter at $Re_c = 204$ and $Re_c = 1632$, respectively. At low Re_c values, a smooth flow contraction takes place, while a condition of *vena contracta* is reached at the largest Reynolds number examined here. In the latter case, small recirculating bubbles are observed adjacent to the walls. The maximum contraction occurs slightly downstream of the entrance, where the fluid stream acquires also its maximum velocity. The size of each recirculating region is approximately $0.062 h_c$. It was confirmed that the removal of the rear plugs has a negligible effect on the flow evolution upstream of the filters and in the region close to the entrance of the inlet channels. Therefore, the results shown in Figure 8 and the above discussion are valid for both the intact filter and the damaged filter with missing rear plugs.

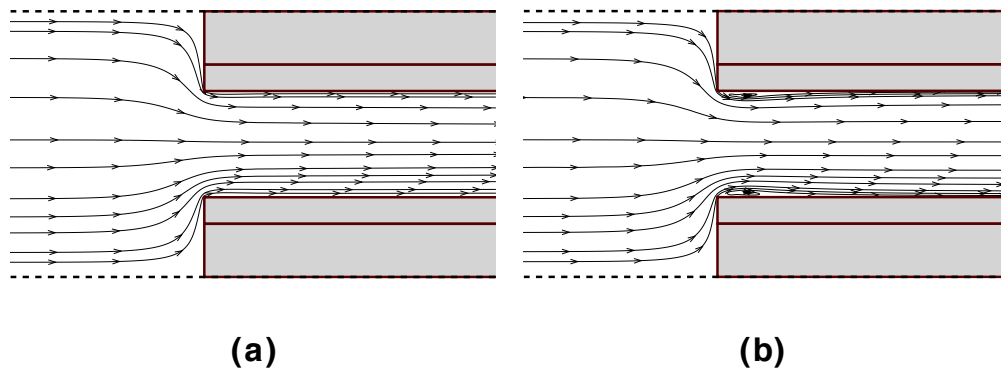


Figure 8. Fluid streamlines near the entrance of the intact filter at $Re_c = 204$ (a) and 1632 (b). The same results are also obtained in the damaged filter without rear plugs.

The effect of the Reynolds number on the fluid velocity at the exit of the intact and damaged filters is illustrated in Figure 9. Regarding the intact filter, Figure 9a clearly demonstrates that a 3D steady and laminar flow is established at $Re_c = 204$. The fluid leaves the outlet channels as coherent jets, whereas a large recirculation may also be seen that covers the whole area of the rear plug. There is no evidence of back-flow at the end of the inlet channels when the Reynolds number is sufficiently small. For comparison purposes, the instantaneous and the time-averaged U velocity at the exit in the case with $Re_c = 1632$ are also shown in Figure 9c,e, respectively. The non-dimensional collection time for the calculation of the mean velocity is $50 h_c / u_0$. It can be seen that the jets have a larger extent in the streamwise direction at the higher Reynolds number, the area with negative values is somehow wider in the y, z -directions and it is located further away from the outer surface of the rear plug. Figure 9c indicates that the jets exhibit oscillations as they are formed in the x -direction. The flow instabilities result in the breakup of the jets downstream of the filter exit, enhancing mixing and fluid turbulence. The aforementioned main flow events at the exit of the intact filter element can be identified in both Figure 9c,e. However, the jets and the recirculation bubble in the time-averaged flow field are smoother than those seen in the instantaneous flow field. It can be noticed that the results up to $X = L_f = 127$ in Figure 9c,e are almost identical to each other, which points out an essentially steady flow inside the inlet and outlet channels of the intact filter.

The removal of the rear plugs has a profound effect on the velocity distribution at the exit of the damaged filter depending on the Reynolds number. Figure 9b reveals that the maximum U velocity (regions in red) associated with the fluid jet exiting from the defective inlet channel is reduced at $Re_c = 204$. There is no indication of any local recirculations. A 3D steady and laminar flow regime prevails at low Re_c values. Figure 9d shows that a turbulent flow is obtained at $Re_c = 1632$, which can be attributed to the spatial growth of instabilities as the central fluid jet evolves downstream of the filter. The central fluid jet appears to be larger in the damaged filter. However, it has lower momentum and, thus, longer distances are required so that it can break up. The jet exiting from the outlet channel has even smaller momentum and flow oscillations are totally absent. The enlargement of the jets is accompanied by a considerable increase of the wake behind the permeable walls (regions in blue). This is an outcome of the fluid mass conservation. In particular, the areas of high U velocity (in red) are accompanied by areas of low U velocity so that the overall mass flow rate in each X location remains constant. Small recirculating areas can also be seen next to the walls. It can be noticed that the characteristics of the time-averaged U velocity are similar to those of the instantaneous velocity as shown in Figure 9f,d, respectively.

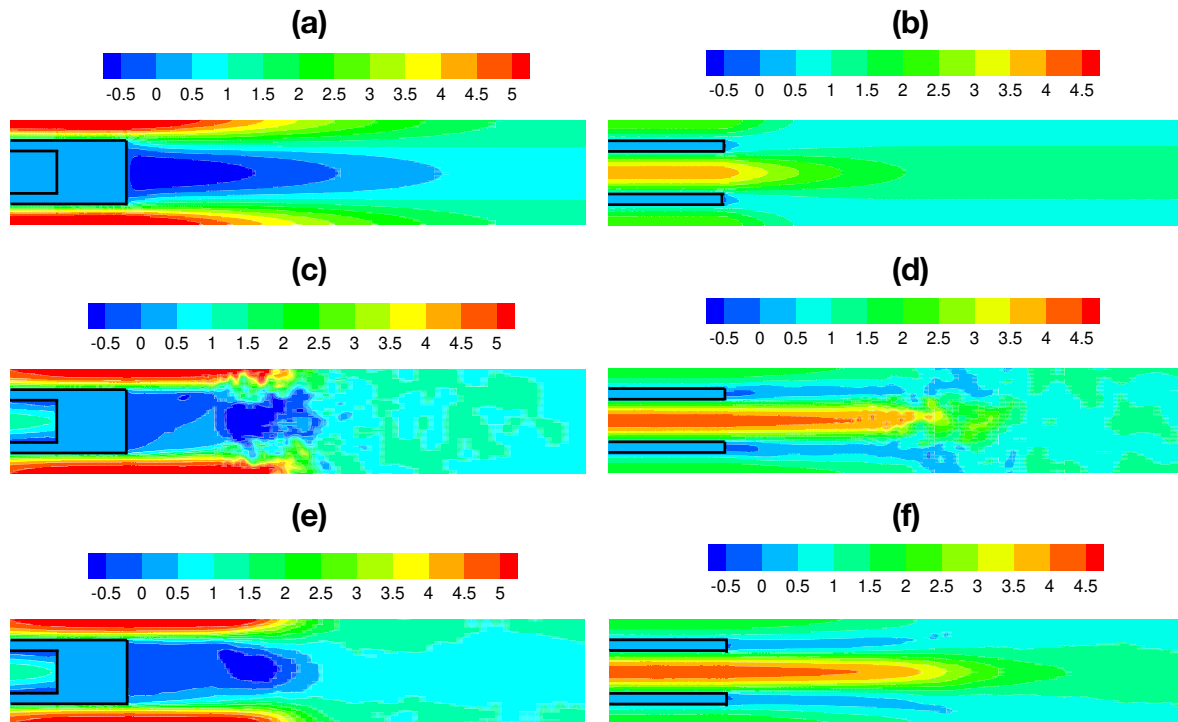


Figure 9. Distribution of the U velocity in the $Y = 1.25$ middle plane for the intact (left column) and damaged (right column) filters at $Re_c = 204$ (upper row) and 1632 (middle and lower rows). The instantaneous U velocity at time $T = 100$ is shown in (a) to (d), and the time-averaged U velocity is shown in (e), (f).

The distribution of the U velocity at both ends, upstream and downstream of the intact filter is consistent with the recent experimental observations of Cooper et al. [18]. The variation of the fluid streamwise velocity inside the inlet and outlet channels is also in qualitative agreement with findings in previous numerical studies [9–11]. Even though the flow in single square channels with impermeable walls has been extensively studied previously (see, for example, Reference [49]), the channel flow changes significantly due to the porous wall boundary condition as discussed above. The present study points out that distinct geometrical imprints on the streamwise fluid velocity exist upstream and downstream of both filters. The imprints are visible at distances approximately up to $10h_c$ from the entrance and exit of the elements, respectively. Such property could possibly be used in the future for flow design and passive control purposes of intact and damaged wall-flow PFs.

The wall permeability may potentially influence the flow features observed in PFs. A weak effect of wall permeability is anticipated here, as indicated by the Reynolds number based on the square root of permeability $Re_{K_w} = \sqrt{K_w}u_{\tau,en}/\nu$ which is smaller than 0.085, where $u_{\tau,en}$ is the wall-friction velocity at the entrance of the inlet channels. Wall roughness can potentially trigger turbulent flow and its effect depends on the Reynolds number $Re_{d_{ob}} = d_{p,ob}u_{\tau,en}/\nu$ which in our case is always $Re_{d_{ob}} \leq 6$. According to Hinze's classification [50], the effect of roughness is negligible when $Re_{d_{ob}} < 5$, while a fully rough wall occurs at $Re_{d_{ob}} \geq 55$. This classification strictly holds for rough and impermeable walls but it also gives a clue in the case where the wall is rough but permeable. Wall roughness is not modeled or taken into account in this work but its effect would be rather insignificant in the cases examined, based on the above analysis. Nevertheless, under different flow conditions and parameters, for example high values of $Re_{d_{ob}}$ and/or Re_{K_w} , wall roughness effects should be expected.

The flow at the end of the filters seems to be comparable to that around rectangular objects. As discussed in Breuer et al. [51], the flow around a single square object is laminar at low Re values and it becomes unsteady as the Reynolds number increases. Such transition from steady to unsteady flow takes place also in the problems under investigation. For example, the flow is laminar

throughout the domain at $Re_c = 204$ and 408 , while a non-homogeneous decaying turbulence is obtained downstream of the intact filter exit at $Re_c = 816$ and 1632 . Similar observations can be made for the damaged filter without rear plugs. However, in this case, the features of turbulence are closer to those in the multi-channel flow of monolithic reactors studied in References [52,53]. It is noted that the flow configurations examined here are far more complex with respect to the flow around rectangular objects due to the permeable walls and the chessboard arrangement of the plugs. Moreover, the actual PF has thousands of channels and the flow at the exit may interact, favoring the development of instabilities and the transition to turbulence.

Figure 10a,b show the variation of pressure in the channels of the intact and damaged filters, respectively. For both geometries, the pressure is reduced more inside the outlet channels. The overall pressure drop is decreased as Re_c is increased, which is more obvious in the intact filter. Abrupt pressure reduction occurs at the entrance of the inlet channels and at the front plugs. In the intact filter, a significant pressure reduction also occurs at the rear plugs. It can be seen that the pressure inside the inlet channels is increased as the rear plug is approached at $Re_c = 408, 816$ and 1632 , which gives rise to the back-flow found in these cases. Figure 10a,b also show the evolution of pressure along the x -direction at the entrance and exit of the filters in the close-up views included in each diagram. At $Re_c = 1632$, a local minimum pressure is observed after the entrance of both filters, as shown in the left zoom window of Figure 10a, which is characteristic of the *vena contracta* condition. It should be noted that this behavior is absent in all the other Re_c cases. Downstream of the filters, pressure fluctuations can be seen as the Reynolds number is increased. For both PFs, it is found that the pressure drop at the entrance is $\Delta P_{ent} = 8.39, 7.43, 6.89,$ and 6.96 at $Re_c = 204, 408, 816,$ and 1632 , respectively. The pressure losses at the exit of the intact filter are $\Delta P_{ex} = 2.96, 2.78, 2.91,$ and 2.87 , while for the damaged filter it holds that $\Delta P_{ex} = 1.09, 1.12, 1.08,$ and 1.34 for $Re_c = 204, 408, 816,$ and 1632 , respectively. It turns out that the pressure losses are larger at the entrance as compared with those predicted at the exit of the filters, whereas ΔP_{ex} is greater for the intact filter.

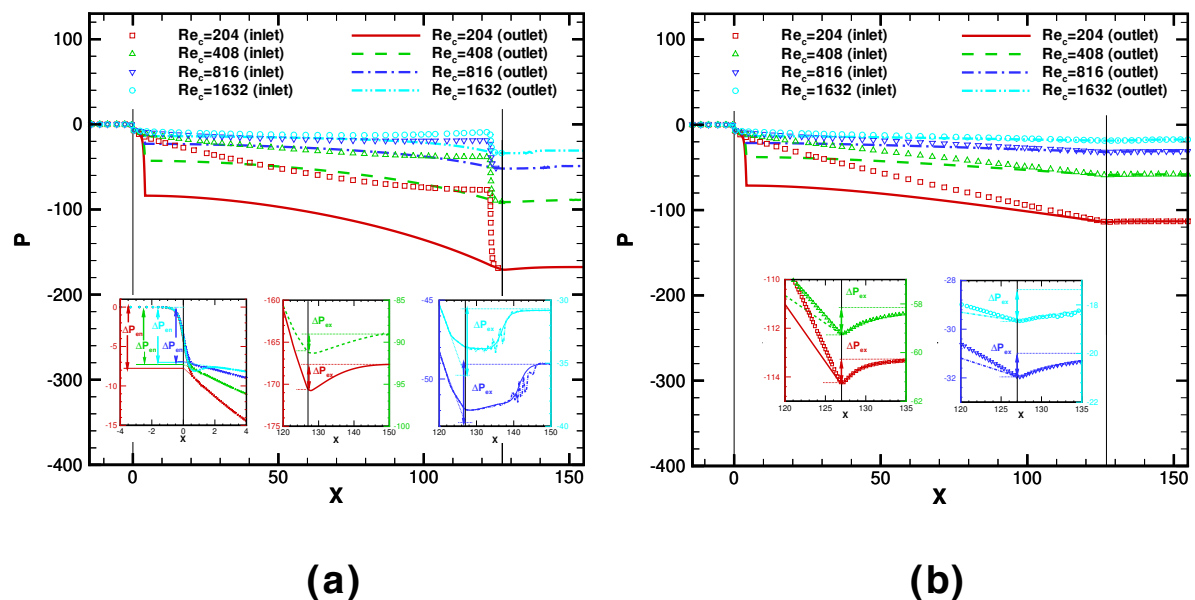


Figure 10. Pressure variation along the x -direction in the inlet and outlet channels of the intact (a) and damaged (b) filter.

5.2. Flow Rates

The results in Figures 7 and 9 point out that the fluid flow is progressively transferred from the inlet to the outlet channels through the porous walls. This also happens, although partially, even in the case without rear plugs. The above observations are confirmed in Figure 11, which shows the variation of the fluid flow rate across the inlet Q_i and the outlet Q_o channels with the normalized distance X/L_f .

Results are presented for both geometries at $Re_c = 204, 408, 816,$ and 1632 . It can be seen that the mass flow rate of the carrier phase is decreased along the x -direction in the inlet channels, while it is increased in the outlet channels.

For the intact filter, the summation of Q_i and Q_o at every X/L_f location is always constant and it equals to the flow rate at the entrance of the inlet channels and at the exit of the outlet channels, $Q_i(X/L_f = 0) = Q_o(X/L_f = 1) = 3.125$. At $Re_c = 204$, an almost linear distribution of Q_i and Q_o can be noticed, and the same flow rate $Q_i = Q_o$ is achieved approximately at the half length of the channels. As the Reynolds number is raised, a weaker reduction (increase) of Q_i (Q_o) is revealed, while the condition $Q_i = Q_o$ is found at distances closer to the end of the inlet channel. Relatively high values of Q_i prevail for longer distances from the entrance, leading to a steeper reduction as the region in front of the rear plug is approached. For the damaged filter, Q_i (Q_o) is attenuated (augmented) slowly toward the exit, which is more noticeable as the Reynolds number is increased. At the same Re_c , the flow rate inside the defective inlet channels is greater relative to the intact inlet channels, while the opposite is true regarding the flow rate inside the outlet channels. The condition $Q_i = Q_o$ is not present when the rear plugs are removed and Q_i is always greater than Q_o for the range of parameters examined here.

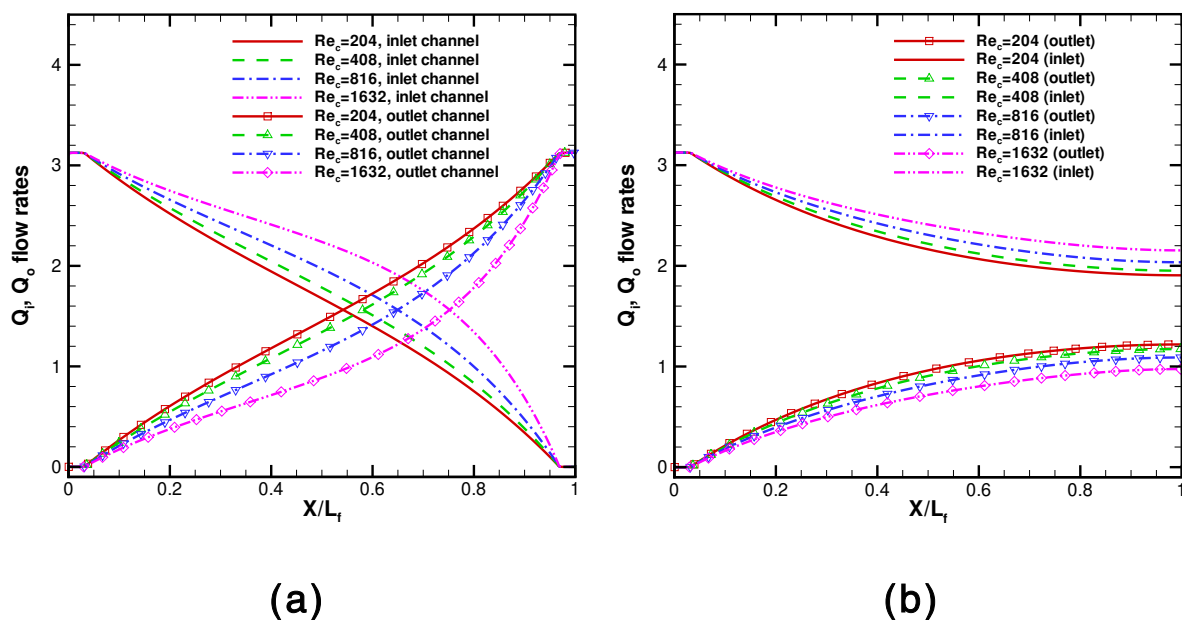


Figure 11. Variation of the flow rate inside the inlet Q_i and outlet Q_o channels along the streamwise direction for the intact (a) and damaged (b) filters.

Figure 12 shows the flow rate through the porous walls Q_w along a pair of channels in the cases with $Re_c = 204, 408, 816,$ and 1632 . In the intact filter, the distribution of Q_w varies non-uniformly in the x -direction, exhibiting two peak values near the ends of the filter, as shown in Figure 12a. The first Q_w peak at the entrance is due to the high velocities of the plug flow profile near the wall. As the flow is steadily modified into an almost parabolic velocity distribution, the near-wall fluid velocities are attenuated and, consequently, the flow rate through the walls is reduced. The second Q_w peak at the exit is attributed to the pressure increase that takes place as the plugged end of the inlet channel is approached, which produces a substantial enhancement of the flow through the walls. The present Q_w profiles are consistent with previous results from 3D CFD simulations [9–12] and simpler 1D models [26] in a different parameter space ($Re_c, \epsilon_w, k_w, h_c, h_w, l_f$ and l_{pl}). The results in Figure 12a suggest that the flow rate through the walls differs with varying Re_c . For example, the magnitude of the Q_w peak value close to $X/L_f = 1$ is greater than that near $X/L_f = 0$ for all the Re_c cases examined here. Since a fixed fluid flow rate passes from the inlet to the outlet channels, the increase of Q_w in the second half of the inlet channels observed with increasing Re_c is accompanied by a reduction in the

rest region. A local minimum value of Q_w is seen around 45% of the filter length for $Re_c = 204$, which is shifted toward the entrance as the Reynolds number is increased, while its magnitude is reduced. The trends found in Q_w may be explained by considering the differences of the pressure inside the inlet and outlet channels. It turns out that the extreme values of the pressure difference between the channels and of Q_w are found at the same locations.

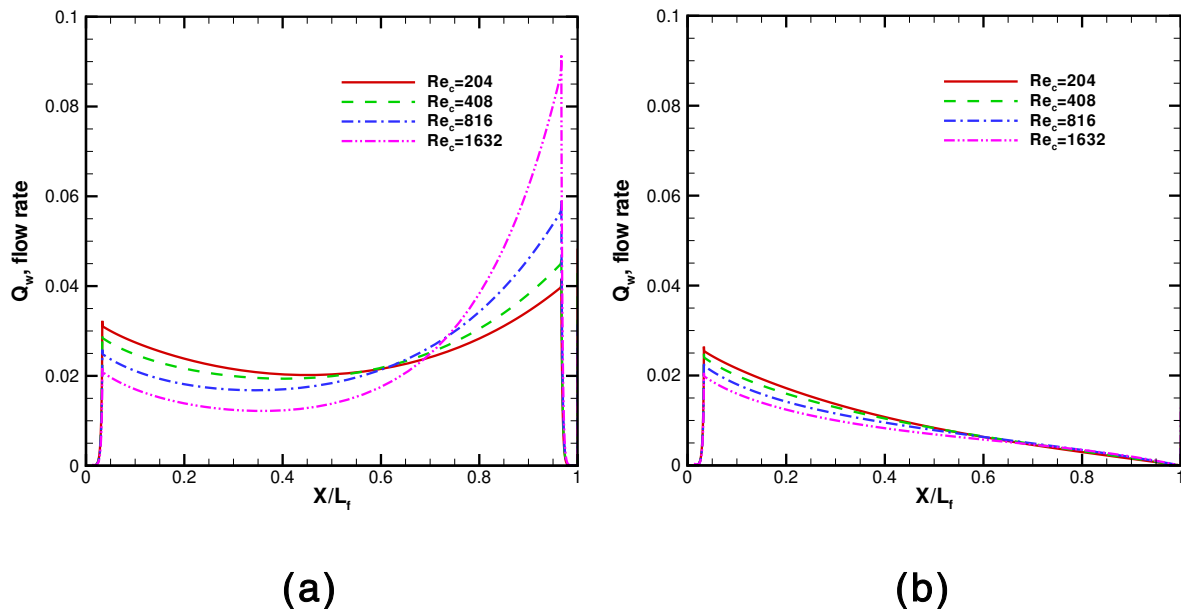


Figure 12. Streamwise variation of the through-wall flow rate Q_w for the intact (a) and damaged (b) filters.

Figure 12b reveals absence of the Q_w peak value at the exit due to the missing rear plugs. In the damaged filter, the pressure difference between the inlet and outlet channels is constantly decreased along the x -direction, and the same pressure is obtained at the exit of the channels. Thus, there is no longer a driving force that creates the flow through the walls and Q_w is diminished at the exit of the defective filter. The Re_c dependence of the Q_w peak near the entrance is similar to that described above for the intact filter. Nevertheless, its magnitude is damped and the overall Q_w is attenuated as Re_c is decreased. This behavior can be associated with the different spatial evolution of the fluid velocity and pressure in the defective inlet channels, as discussed in Figures 7–10. Figure 12b indicates that less fluid crosses the permeable walls relative to the intact filter, which explains the lower flow rates achieved along the outlet channels, as well as the weaker fluid jets coming out from the unplugged inlet channels. Similar Q_w profiles have been obtained previously by utilizing 1D models [24–26], while there are no results from 3D CFD studies. The present work provides further insight into the 3D features of the fluid flow in defective filter channels without rear plugs, which can potentially lead to non-uniform particle deposition.

5.3. Particle Transport and Deposition

Figure 13 shows a visual impression of the instantaneous positions of particles having diameter $d_p = 200$ nm in the intact and damaged filters at representative time instances T_i ($i = 0, 1, 2, \dots, 8$). For the intact filter, the particles are uniformly introduced in the computational domain from the inflow boundary (T_0) as shown in Figure 13a. They are transported by the fluid flow, maintaining an almost uniform distribution upstream of the filter ($T_1 - T_3$), while part of the particles moves toward the central region of the entrance (T_4). The particles located initially in the innermost zone of the inlet channel move longer distances in the x -direction, due to the greater fluid velocities there. In addition, the particles travel toward the permeable walls, because of the transverse fluid velocities that develop in the inlet channels. As an outcome of these combined fluid motions, the particles are concentrated

in certain flow regions forming a paraboloid. The instantaneous particle positions look closely like the distributions of the streamwise fluid velocity, and their evolution at different times ($T_5 - T_7$) is quite similar to the fluid flow evolution in the x -direction from a plug into a laminar parabolic profile. The particle stream reaches the rear plug (T_7) and eventually the population of particles is reduced significantly owing to their deposition (T_8).

The same observations can also be made for the time evolution of the particle positions in the damaged filter, especially at the early stages of particle dispersion ($T_0 - T_6$), as shown in Figure 13b. However, the removal of the rear plugs permits the particles to exit from the defective channels (T_7, T_8). After some time, all the particles that have not deposited leave the computational domain from the outflow boundary. As discussed above, the fluid velocity field obtained in the damaged filter differs from that in the intact filter, which is reflected on the different spatial distribution of the particles between the two cases ($T_4 - T_6$).

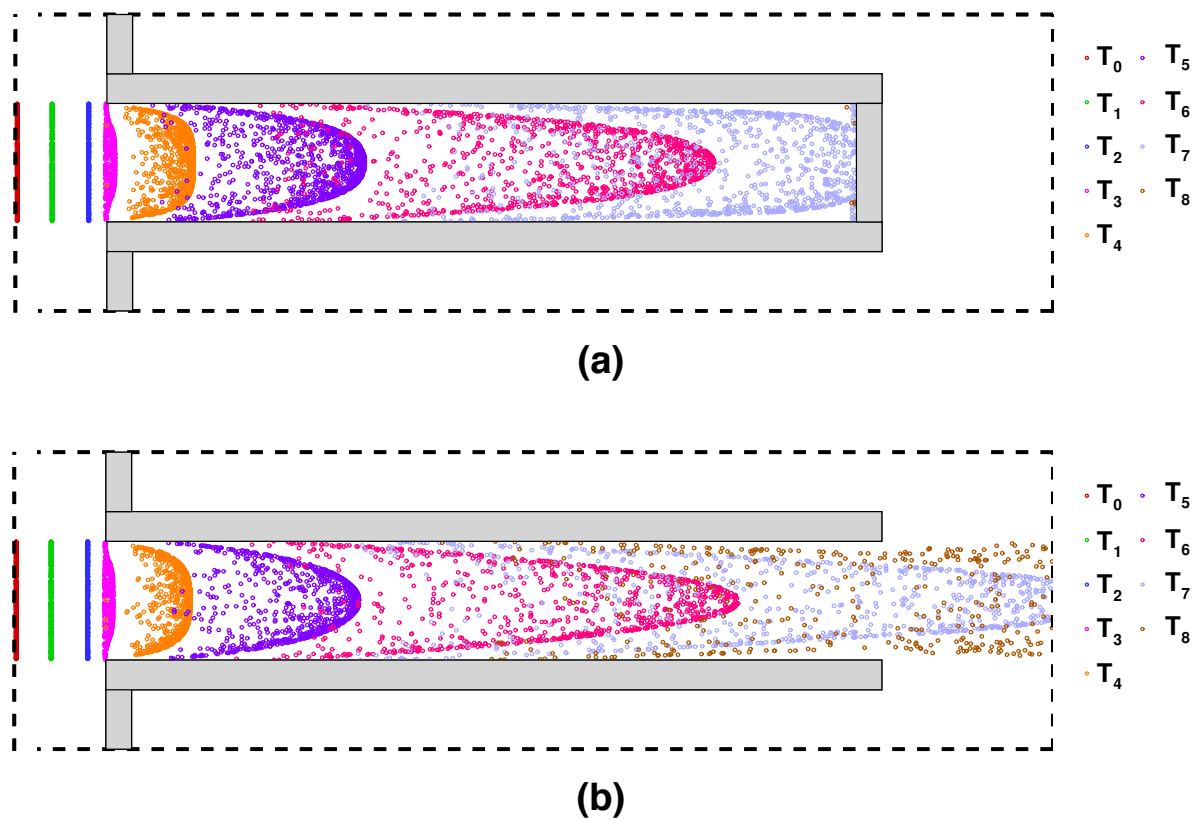


Figure 13. Evolution of instantaneous positions of particles having diameter $d_p = 200$ nm and Stokes number $St = 1.5 \times 10^{-3}$ in the intact (a) and damaged (b) filters at $Re_c = 1632$. The time instances are $T_0 = 0$, $T_1 = 0.2 \times 10^4 St$, $T_2 = 0.4 \times 10^4 St$, $T_3 = 0.5 \times 10^4 St$, $T_4 = 0.6 \times 10^4 St$, $T_5 = 0.8 \times 10^4 St$, $T_6 = 1 \times 10^4 St$, $T_7 = 1.75 \times 10^4 St$, and $T_8 = 2.25 \times 10^4 St$.

To gain further insight into the particle transport by the carrier fluid flow, Figure 14 shows characteristic trajectories of particles with $d_p = 200$ nm at $Re_c = 1632$. In the flows examined here, high transverse fluid velocities are generated in the inlet channels and the fluid passes through the permeable walls. Consequently, the fluid streamlines are not parallel to the surface of the porous walls and plugs but they cross it. Small size particles are capable of responding quickly to all changes of the fluid flow. The response times of the particles used in the simulations are $\tau_p = 1.23 \times 10^{-9}$, 6×10^{-9} , and 3.39×10^{-9} s that correspond to Stokes numbers $St_c = \tau_p u_c / h_c$ in the range of $6.82 \times 10^{-6} \leq St_c \leq 1.5 \times 10^{-3}$. It is clear that such low response time particles under the effect of drag force and inertia tend to follow closely the fluid streamlines. This behavior of particles is not considerably altered by the inclusion of the Brownian force terms, at least from a macroscopic viewpoint (see, for example,

References [9,54]). The transverse fluid velocities become weaker in the defective inlet channels and only a part of the fluid flows through the walls into the outlet channels. The streamlines between the intact and damaged filters are dissimilar to each other, as a consequence of the different hydrodynamic flow fields in these cases. This unlikeness is expected to be reflected on the particle trajectories.

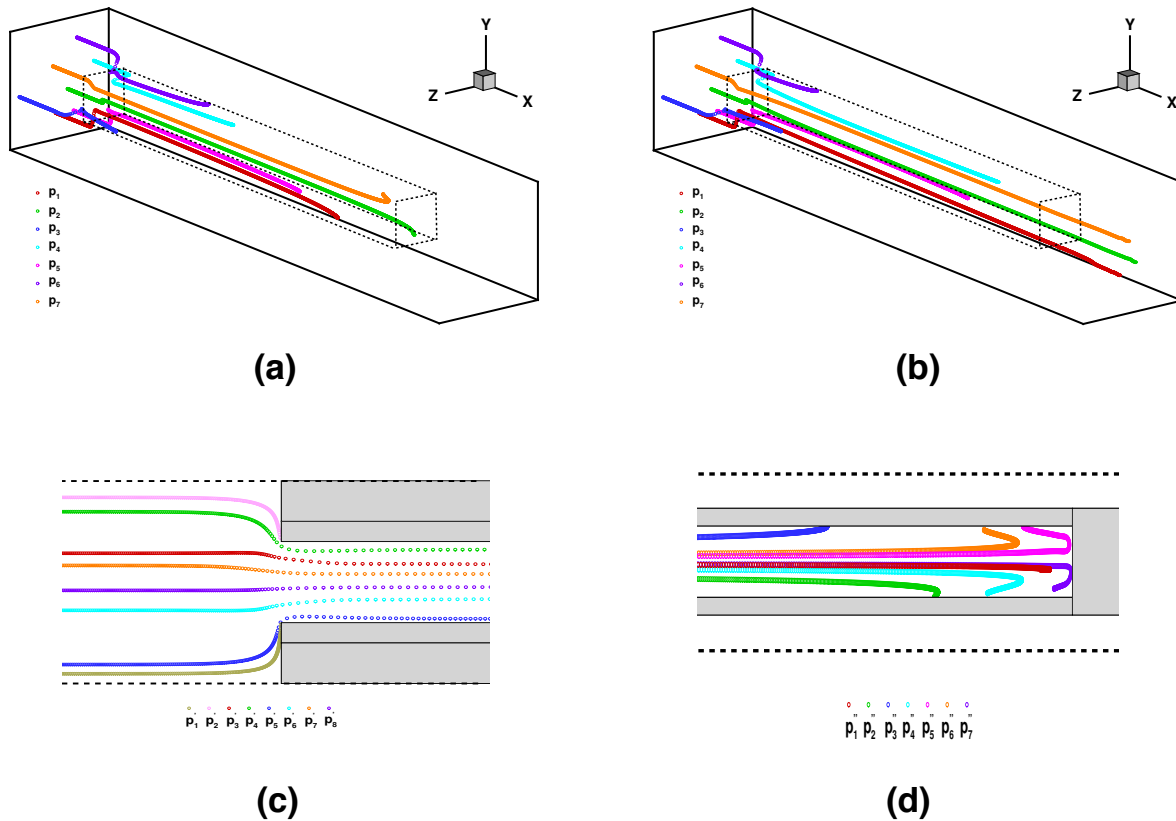


Figure 14. Sample of seven 200 nm particle trajectories (p_1 to p_7) in the intact (a) and damaged (b) filters. Side x - y view of the particle trajectories at the entrance (p'_1 to p'_8) (c) and end of the intact inlet channel (p''_1 to p''_8) (d). The particle trajectories in front of the damaged filter are the same to those shown in (c). For both intact and damaged filters, the particles are introduced in the flow domain at the same position. The initial particle velocity equals to that of the carrier phase at the position where the particles are released.

For the intact filter, Figure 14a shows that initially the particle paths bend inward at the entrance of the inlet channel due to the flow contraction. This can be appreciated better in Figure 14c, which reveals that the particle trajectories at the entrance are similar to the fluid streamlines there (see Figure 8). Most of the particles are carried in the filter (p'_3 to p'_8), whereas, under certain conditions, some of them may follow the fluid streamlines that go through the frontal face of the filter, where they are deposited (p'_1, p'_2). Inside the inlet channel, the particles are effectively transferred by the underlying fluid motions toward the porous walls. The locations at which the particles hit the walls vary in the x -direction, as indicated in Figure 14a. This can be attributed to the fact that the cross-flow fluid motions are relatively weak away from the walls and, thus, the particles that enter from the central region of the inlet channels are most likely to travel longer distances in the streamwise direction. Figure 14d indicates that the back-flow observed at the end of the inlet channels at $Re_c = 1632$ (see Figures 7 and 9) affects significantly the motion of the particles (p''_1, p''_4 to p''_8), and it can potentially control the number of particles that impact the rear plugs. Away from the channel end, the back-flow is not strong enough to produce a noticeable effect on the particle path-lines (p''_2, p''_3). The effect of the missing rear plugs on the particle transport is demonstrated in Figure 14b. It is seen that the particle path-lines from the inflow boundary up to the entrance of the flawed inlet channel are identical

to those described for the intact filter. On the other hand, the locations of the deposited particles inside the inlet channel are obviously different between the two cases (p_3 to p_6). This is because of the discrepancies in the velocity and pressure fields between the two configurations at a certain Reynolds number. Figure 14b also shows the trajectories of some particles that escape from the unplugged inlet channel (p_1 , p_2 , and p_7).

Next, we try to characterize and quantify the deposition of nanoparticles in the intact and damaged filters. The positions at which $d_p = 200$ nm particles deposit at the walls of the intact filter are shown in Figure 15a,c, respectively. The data in these figures correspond to the positions where the particles hit the two x - y channel sides. Figure 15b,d show the probability density function (*PDF*) of the deposited particles as a function of the x -direction. The *PDF* has been computed by counting the number of particles N_d that impact each of the four channel walls within specified intervals in the streamwise direction, normalized by the total number of deposited particles $N_{d,tot}$. This quantity may be considered a more quantitative way to describe the variation of particle deposition along the length of the inlet channel.

Figure 15b reveals that the particles are deposited almost uniformly over a large extent of the inlet channel at $Re_c = 204$. Two small peak values of the *PDF* appear near both ends of the channel. On the other hand, it is evident in Figure 15d that the vast majority of the particles are deposited preferentially at the end of the inlet channel at $Re_c = 1632$. A smaller peak value of the *PDF* also occurs near the entrance of the filter. The x variation of $PDF(N_d/N_{d,tot})$ resembles closely the distribution of the through-wall flow rate Q_w that is also shown in these figures. This similarity suggests that the convective fluid transport toward the permeable walls is the key mechanism that controls the particle deposition in the intact filter (see, for example, References [9,10]) At $Re_c = 204$, the locations of deposited particles are uniformly distributed at the walls in the spanwise direction, as shown in Figure 15a. The 200 nm particles are capable of responding even to relatively weak transverse fluid motions that can transfer them toward the walls. At $Re_c = 1632$, the Stokes number is increased, which points out that more momentum is required so that the particles can reach the walls. Figure 15c indicates that the particles impact the walls on positions that are non-uniformly spread, exhibiting a somehow greater tendency to deposit at regions closer to the corners of the channel. The through-wall flow at the corners is an outcome of the contribution of both cross flow y and z velocity components, resulting in a higher flow rate through the permeable walls and, subsequently, an enhanced local particle deposition.

These observations are consistent with the findings of Sbrizzai et al. [9], while the present study provides further results for the Reynolds number effect on the spatial distribution of deposited particles in the streamwise and spanwise directions. It turns out that the Stokes number for a specific particle set decreases with increasing Reynolds number, producing an overall effect on the particle deposition that is similar, at least from a statistical point of view, to that observed when the size of particles is decreased while the Reynolds number is kept constant.

Figure 16 shows the positions of deposited particles and the distribution of $PDF(N_d/N_{d,tot})$ in the case of damaged filter at $Re_c = 204$ and 1632. The similarity between $PDF(N_d/N_{d,tot})$ and Q_w distributions still holds, although to a lesser extent, irrespective of the missing rear plugs as shown in Figure 16b,d. For all the Re_c cases examined, the *PDF* obtains larger values in the initial portion of the inlet channel and zero close to the channel exit. It can be seen that the peak value of the *PDF* is shifted further away from the entrance with increasing Reynolds number. It is noted that this behavior is also observed in the intact filter in Figure 15b,d but it is less pronounced. These findings point out that the through-wall flow plays an important role in the particle deposition in the damaged filter without rear plugs. However, this deposition mechanism is less effective as compared with the case of intact filter. Consequently, the population of deposited particles is significantly attenuated, as shown in Figure 16a,c, especially at $Re_c = 1632$.

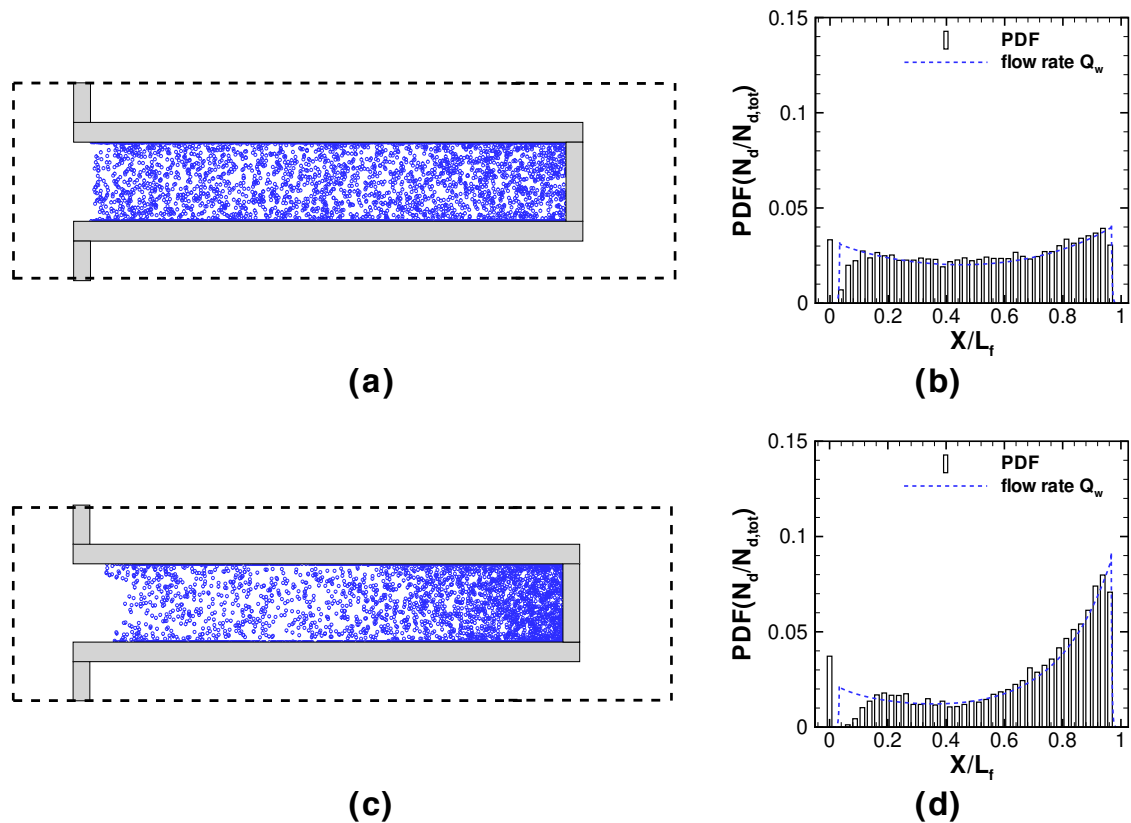


Figure 15. Side x - y view of the locations of deposited particles (a), (c) and the probability density function of particle deposition number inside the inlet channel of the intact filter (b), (d). Results correspond to particles with $d_p = 200$ nm at $Re_c = 204$ (a), (b) and 1632 (c), (d). For clarity, one in every ten deposited particles is shown.

Based on the results shown in Figures 13–16, it can be inferred that the behavior of the particle-laden flow upstream of the PFs is not influenced by the presence of the rear plugs. The present study provides evidence that a significant amount of particles is deposited at the front area of the filters, as indicated by the non-zero value of the PDF for $X/L_f < 0$ (first bar in Figures 15b,d and 16b,d). For both the intact and damaged filters, it is found that 3.4% and 4.7% of particles with $d_p = 200$ nm impact the frontal face at $Re_c = 204$ and 1632, respectively. This denotes that particle deposition at the front area of the filters is enhanced as the Reynolds number is raised. It should be noted that the different values of the PDF for $X/L_f < 0$ between the intact and damaged filters at a fixed Re_c are because $N_{d,tot}$ in the latter case generally differs with varying Reynolds number, whereas N_d is the same.

To obtain a clearer picture regarding the particle deposition on the frontal area of the PFs, we examine the locations of deposited particles at $Re_c = 204$ and 1632, which are shown in Figure 17a,b, respectively. Results are presented for the intact filter, but exactly the same analysis also holds for the damaged filter. A significant accumulation of particles is apparent at the edges of the entrance. This is because the particles are transferred by the carrier phase following streamlines that cross the permeable plugs and walls, as illustrated in Figure 17c. The streamlines correspond to the $Z = 1$ plane, at which the particle trajectories are projected. The small deviation observed between the particle trajectories and the streamlines close to the front porous wall is because the particles are actually deposited at a different z plane, and in lower degree due to the random shift introduced to the impact location by the Brownian force terms. The deposition of nanoparticles, especially at the filter entrance, may lead to the formation of complicated dendrites. Their presence will certainly affect the fluid flow inside the channels, the pressure losses, and the particle collection efficiency. The local recirculating bubbles observed at the entrance of the intact and damaged filters at $Re_c = 1632$ are isolated from the

rest of the flow. These are surpassed by the fluid streamlines entering the channels and, thus, they cannot interact with or capture the dispersed particles. The same also holds for the recirculations at the exit of the PFs. However, the presence of recirculations has a pronounced effect on the distributions of velocity and pressure and, thus, they affect indirectly particle deposition.

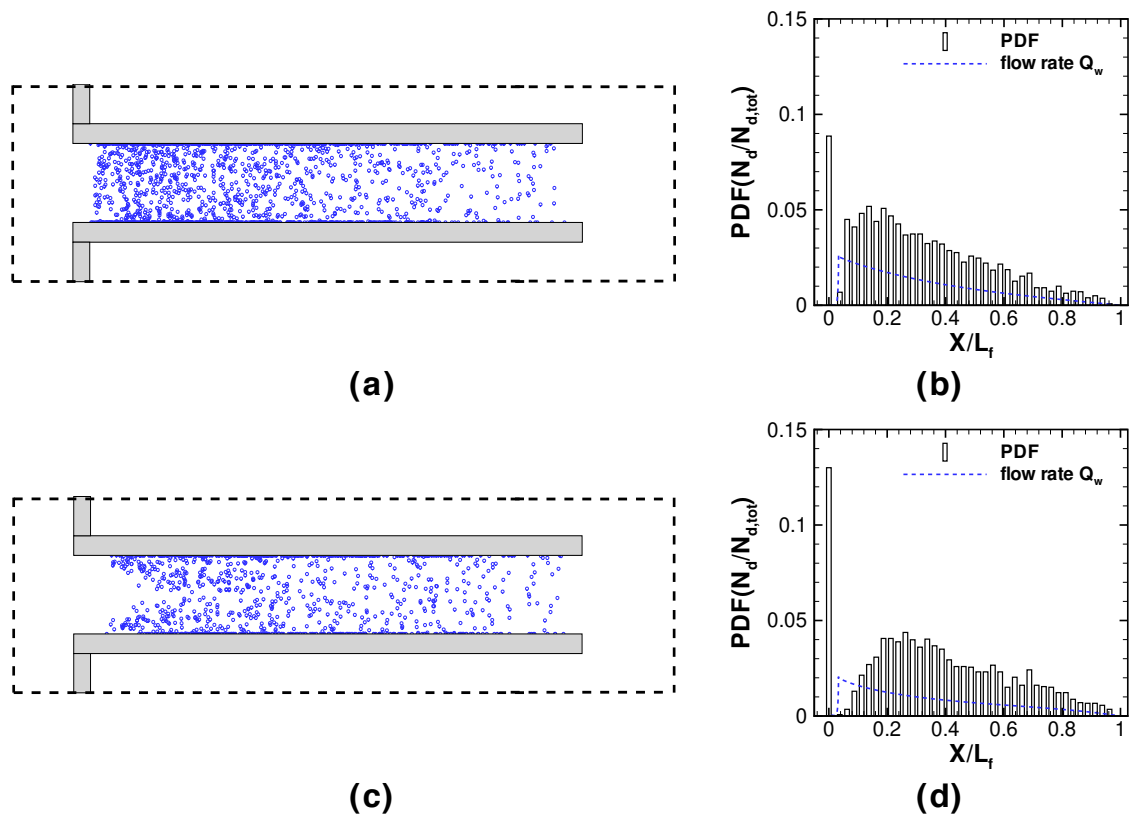


Figure 16. Side x - y view of the locations of deposited particles (a), (c) and the probability density function of particle deposition number inside the inlet channel of the damaged filter (b), (d). Results correspond to particles with $d_p = 200$ nm at $Re_c = 204$ (a), (b) and 1632 (c), (d). For clarity, one in every ten deposited particles is shown.

The numerical results on the particle deposition process in intact filters and damaged filters with missing plugs are consistent with recent experimental findings [43]. For instance, the experiments indicate clearly that the deposit soot accumulates almost uniformly in the central region of the intact filter, whereas the deposit loading is gradually reduced from the entrance of the defective filter obtaining a zero value at its exit. The present work focuses on the investigation of particle transport and deposition at low filtration times in clean PFs. Under such conditions, it is reasonable to assume that the distribution of the particle mass flow rate toward the walls will look like the through-wall velocity profile [10]. The majority of previous 3D numerical studies predict two peak values in the through-wall velocity profile at the ends of the intact filter (see, for example, References [9–12]). They also indicate that a non-homogeneous deposition of particles occurs along the filter length. However, enhanced particle deposition at the entrance and end of the inlet channel is found in some works [10–12], while high soot concentration only at the end of the inlet channel is anticipated in other studies [9]. The flow contraction that takes place at the filter entrance can potentially influence the location at which particle deposition begins. The size of the plugs and whether they are permeable or not can also affect the particle behavior in the entrance flow region of the filter. The present study provides for the first time numerical results of particle deposition at the frontal surface of the wall-flow filter, which are consistent with visual observations from experiments (see, for example, Reference [43]).

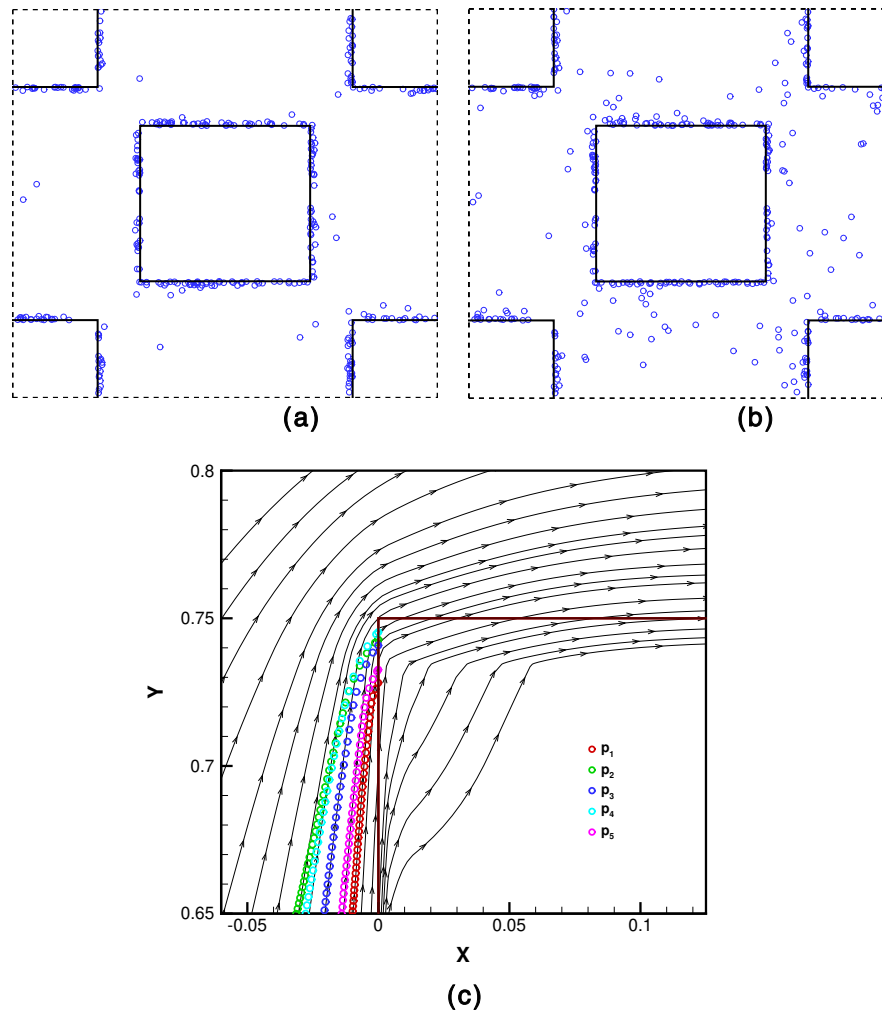


Figure 17. Locations of deposited particles with $d_p = 200$ nm in the front area of the intact filter at $Re_c = 204$ (a) and 1632 (b). Fluid streamlines at the $Z = 1$ plane near the filter entrance at $Re_c = 204$ and several representative particle trajectories p_i ($i = 1, 2, 3, 4, 5$) (c). The same results are obtained in the case of damaged filter.

The removal of the rear plugs leads to a considerable particle leakage that has to be determined and quantified. Figure 18 shows the efficiency of the damaged filter, the number of particles that are captured by the porous walls, as a function of the Reynolds number for the three particles sets with $d_p = 20, 60,$ and 200 nm. It is defined as $E = N_d/N_{tot}$, where N_d is the number of deposited particles and N_{tot} is the number of total particles tracked in the simulations. As Re_c is increased, fewer particles are generally deposited, since the transverse fluid motions inside the unplugged inlet channels are moderate and, thus, they transfer less effectively the particles near to the walls. Moreover, the Stokes number is increased with increasing Reynolds number, and the particles become relatively unresponsive to the surrounding flow changes and follow less closely the local through-wall flow that controls their deposition. Similarly, the increase of particle size augments the Stokes number and, consequently, it increases particle leakage from the damaged filter.

The same scenario is also valid for the particle deposition in the front face of the filters. In particular, the flow rate corresponding to the fluid motions that cross the frontal surface is relatively small. Thus, smaller size particles are more capable of gaining sufficient momentum from the carrier phase in order to reach the front area as compared with the larger size particles. The particles with $d_p = 200$ nm have a very low response time so that their trajectory approximates the underlying fluid motions. However, the trajectory of such particles may intercept with the front surface in locations away from the edges of the channel entrance due their greater size, resulting in a non-uniform scatter

of the impact positions. In contrast to what happens inside the channels, the fluid flow upstream of the filter elements acquires more momentum as the Reynolds number is raised. Thus, the fluid motions associated with the convective transfer toward the frontal face become stronger and, eventually, local particle deposition is enhanced for the whole spectrum of particle response times and sizes examined here. Consequently, a different Re_c dependence of the efficiency is obtained regarding the particle deposition process in the frontal face of the filters, which is also shown in Figure 18.

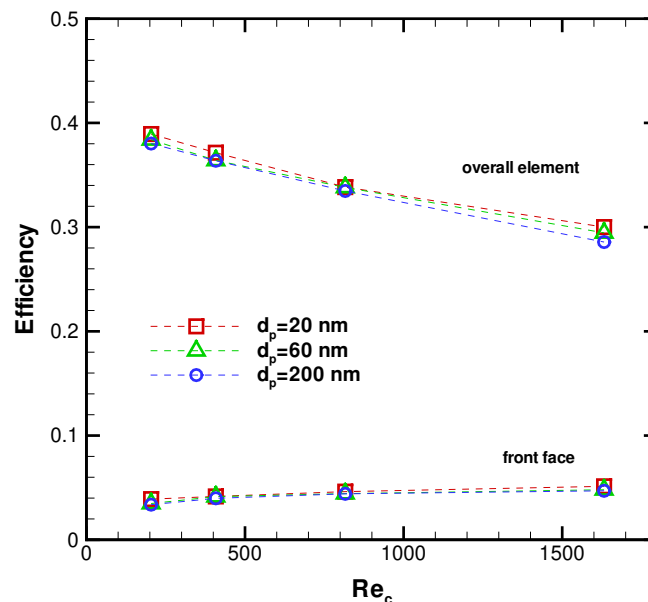


Figure 18. Efficiency of particle capture in the overall element and in its frontal surface as a function of the Reynolds number in the damaged filter without rear plugs.

6. Conclusions

We have investigated the time-dependent 3D particulate flow in intact filters and partially damaged filters in which the rear plugs have been removed. For the purposes of this study, we accounted for the flow in the clear fluid region and the permeable walls and plugs by solving the Navier–Stokes equations and the volume-averaged Navier–Stokes equations based on the Brinkman model with an additional Forchheimer term, respectively. Discrete particle simulation was utilized to model the dynamic behavior of the suspended nanoparticles in rarefied gas flow regimes for the two filters. The particle trajectories were determined based on the drag force that accounts for the partial slip effect and the Brownian motion. We performed extensive comparisons in representative flow cases, in order to verify the validity of the developed code and then we conducted a grid sensitivity analysis to ensure grid convergence of the present results. The main interest of this work was focused on addressing the differences in the flow pattern for representative Reynolds number in the range of $204 \leq Re_c \leq 1632$ and the deposition process of mono-dispersed ensembles of particles having diameters $d_p = 20, 60,$ and 200 nm between the intact and the damaged filter elements.

We presented iso-contours of the fluid velocity which describe the main flow features developing inside the channels and in areas upstream and downstream of them. This assisted the identification of those particular flow characteristics that affect the transport and deposition of the particles.

For both geometries, a smooth flow contraction takes place in the entrance, while local recirculating bubbles appear adjacent to the walls and the fluid stream obtains its smallest area, a local maximum velocity and a local minimum pressure, reaching a condition of *vena contracta* at the largest Reynolds number examined here.

The plug flow observed at the entrance of the inlet channels evolves into a laminar parabolic distribution that is completely weakened in front of the rear plug, forcing the fluid to pass through the permeable walls into the outlet channels. Our results provide evidence of pressure increase at the end

of the inlet channels at $Re_c = 408, 816$ and 1632 , leading to a considerable back-flow. The flow transfer across the porous walls is relatively uniform along the axial flow direction at low Reynolds numbers and it becomes highly non-uniform at large Re_c values, exhibiting two peak values at the entrance and the end of the inlet channel. The minimum flow rate is found in the middle of the channel length that is attenuated and shifted toward the entrance with increasing Reynolds number.

The removal of the rear plugs results in a different velocity distribution inside the channels allowing the fluid flow to exit from the defective inlet channels at greater rates as compared with the outlet channels. The overall pressure losses at the exit are smaller relative to those found in the intact filter element. The flow modifications, which depend on the Reynolds number, are reflected on the spatial distribution of the through-wall flow rate that obtains a local peak value near the entrance of the damaged filter and it is gradually diminished as the exit is approached.

At the region downstream of both filters, the flow exits in the form of strong coherent jets that are accompanied by recirculating bubbles. At certain distances from the exit and at certain flow parameters, the jets may break up, enhancing mixing and favoring transition to turbulence. The size and strength of the jets and the recirculating regions, as well as the characteristics of the achieved turbulence differ between the intact and the damaged filters.

The above mentioned flow features agree reasonably well with previous numerical studies [9–14] and that they have been identified in recent experiments [18].

We described the particle trajectories and show that the particles follow closely the streamlines of the carrier fluid flow. $St \ll 1$ generally holds and, thus, the particles respond quickly to all scales of fluid motion. High transverse fluid velocities develop inside the intact and unplugged inlet channels due to the presence of the permeable walls. As an outcome, the streamlines are not parallel to the walls and plugs but they may cross them.

The positions of the particles evolve in time in a similar manner to the variation of the streamwise fluid velocity in the x -direction. Thus, the differences of velocity fields between the intact and the damaged filters at the same Reynolds number are reflected on the spatial distribution of the particles. The removal of the rear plugs allows a considerable number of nanoparticles to escape from the defective channels, reducing the filtration efficiency.

We characterized the particle deposition in the intact and damaged filters. The convective fluid transport toward the porous wall is the key mechanism that controls particle transfer and deposition for both filters. The deposited particles are distributed along the filter length in a similar way to the streamwise variation of the through-wall velocity. For the intact filter, the particle concentration obtains large values near the entrance and exit of the inlet channel. For the damaged filter, high particle concentration is observed close to the channel entrance and it is diminished at the exit.

We also investigated the particle deposition on the frontal surface of the filters. A noticeable particle accumulation occurs at the edges of the filter entrance, which is enhanced for particles with low response times in flows with high flow rates.

We examined and quantified the particle leakage due to the removal of the rear plugs. Fewer particles are captured in the damaged filter with increasing Reynolds number and particle response time owing to the augmented unresponsiveness of the particles to the local flow changes.

Author Contributions: Conceptualization and planning of the work presented in the manuscript by all contributing authors. C.D.D. developed the code and did the simulations. C.D.D. and F.T. prepared the draft manuscript. F.T. and M.M. performed post-processing of results. O.H. edited the final draft of the manuscript and supervised this work.

Funding: This research is co-financed by Greece and the European Union (European Social Fund-ESF) through the Operational Programme “Human Resources Development, Education and Lifelong Learning 2014–2020” in the context of the project “Microscale Computational and Experimental Investigation of the Behavior of Partially Failed Particulate Filters” (MIS 5007658).

Acknowledgments: The authors are indebted for the opportunity to perform some of the large-scale simulations to the cluster facilities of University of Thessaly and of University of West Attica.

Conflicts of Interest: The authors declare no conflict of interest.

References

1. Bissett, E.J. Mathematical model of the thermal regeneration of a wall-flow monolith diesel particulate filter. *Chem. Eng. Sci.* **1984**, *39*, 1233–1244. [[CrossRef](#)]
2. Haralampous, O.A.; Koltsakis, G.C. Back-diffusion modeling of NO₂ in catalyzed diesel particulate filters. *Ind. Eng. Chem. Res.* **2004**, *43*, 875–883. [[CrossRef](#)]
3. Guo, Z.; Zhang, Z. A one-dimensional numerical model for diesel particulate trap performance study during loading and regeneration. *Int J. Engine Res.* **2005**, *6*, 247–262. [[CrossRef](#)]
4. Depcik, C.; Assanis, D. Simulating area conservation and the gas-wall interface for one-dimensional based diesel particulate filter models. *J. Eng. Gas Turb. Power* **2008**, *130*, 062807. [[CrossRef](#)]
5. Piscaglia, F.; Ferrari, G. A novel 1D approach for the simulation of unsteady reacting flows in diesel exhaust after-treatment systems. *Energy* **2009**, *34*, 2051–2062. [[CrossRef](#)]
6. Torregrosa, A.J.; Serrano, J.R.; Arnau, F.J.; Piqueras, P. A fluid dynamic model for unsteady compressible flow in wall-flow diesel particulate filters. *Energy* **2011**, *36*, 671–684. [[CrossRef](#)]
7. Koltsakis, G.; Haralampous, O.; Depcik, C.; Ragone, J.C. Catalyzed diesel particulate filter modeling. *Rev. Chem. Eng.* **2013**, *29*, 1–61. [[CrossRef](#)]
8. Konstandopoulos, A.; Skaperdas, E.; Warren, J.; Allansson, R. Optimized filter design and selection criteria for continuously regenerating diesel particulate traps. *SAE Tech.* 1999, *108*, 279–288.
9. Sbrizzai, F.; Faraldi, P.; Soldati, A. Appraisal of three-dimensional numerical simulation for sub-micron particle deposition in a micro-porous ceramic filter. *Chem. Eng. Sci.* **2005**, *23*, 6551–6563. [[CrossRef](#)]
10. Bensaid, S.; Marchisio, D.; Fino, D.; Saracco, G.; Specchia, V. Modelling of diesel particulate filtration in wall-flow traps. *Chem. Eng. J.* **2009**, *154*, 211–218. [[CrossRef](#)]
11. Bensaid, S.; Marchisio, D.L.; Fino, D. Numerical simulation of soot filtration and combustion within diesel particulate filters. *Chem. Eng. Sci.* **2010**, *65*, 357–363. [[CrossRef](#)]
12. Lee, H.; Lee, K.O. Multi-layered mesh generation and user subroutine development based on an Eulerian–Eulerian approach for soot filtration visualization in a three-dimensional particulate filter model. *Int. J. Engine Res.* **2014**, *15*, 980–992. [[CrossRef](#)]
13. Konstandopoulos, A.; Skaperdas, E.; Masoudi, M. Inertial contributions to the pressure drop of diesel particulate filters. In Proceedings of the SAE 2001 World Congress, Detroit, MI, USA, 5–8 March 2001; 2001-01-0909.
14. Liu, Z.; Miller, R. Flow distributions and pressure drops of wall-flow diesel particulate filters. In Proceedings of the SAE 2002 World Congress & Exhibition, Detroit, MI, USA, 4–7 March 2002; 2002-01-1311.
15. Opris, C.; Johnson, J. A 2-D Computational model describing the flow and filtration characteristics of a ceramic diesel particulate trap. In Proceedings of the SAE International Congress & Exposition, Detroit, MI, USA, 23–26 February 1998; 980545.
16. Deuschle, T.; Janoske, U.; Piesche, M. A CFD-model describing filtration, regeneration and deposit rearrangement effects in gas filter systems. *Chem. Eng. J.* **2008**, *135*, 49–55. [[CrossRef](#)]
17. Sarli, V.D.; Benedetto, A.D. Modeling and simulation of soot combustion dynamics in a catalytic diesel particulate filter. *Chem. Eng. Sci.* **2015**, *137*, 69–78. [[CrossRef](#)]
18. Cooper, J.D.; York, A.P.E.; Sederman, A.J.; Gladden, L.F. Measuring velocity and turbulent diffusivity in wall-flow filters using compressed sensing magnetic resonance. *Chem. Eng. J.* **2019**, *377*, 119690. [[CrossRef](#)]
19. Koptuyug, I.; Altobelli, S.; Fukushima, E.; Matveev, A.; Sagdeev, R. Thermally polarized 1H NMR microimaging studies of liquid and gas flow in monolithic catalysts. *J. Magn. Reson.* **2000**, *147*, 36–42. [[CrossRef](#)]
20. Ramskill, N.P.; York, A.P.E.; Sederman, A.J.; Gladden, L.F. Magnetic resonance velocity imaging of gas flow in a diesel particulate filter. *Chem. Eng. Sci.* **2017**, *158*, 490–499. [[CrossRef](#)]
21. Samaras, Z. *On Board Diagnostics Legislation for Euro 6/VI Light and Heavy Duty Vehicles in Europe*; On-Board Diagnostics Symposium: Indianapolis, IN, USA, 2010.
22. Finch, S.; Hnilicka, B.; Sindano, H. *EURO6 Light Duty Vehicle OBD Project: Evaluation and Assessment of Proposed EOBD Emission Thresholds*; ACEA-Commissioned Report Q51760, RD.10/320201.4; ACEA: Brussels, Belgium, 2010.

23. Basu, S.; Henrichsen, M.; Tandon, P.; He, S.; Heibel, A. Filtration efficiency and pressure drop performance of ceramic partial wall flow diesel particulate filters. *SAE Int. J. Fuels Lubr.* **2013**, *6*, 877–893. [[CrossRef](#)]
24. Haralampous, O.; Kontzias, T. Approximate pressure drop and filtration efficiency expressions for semi-open wall-flow channels. *Canad. J. Chem. Eng.* **2014**, *92*, 1517–1525. [[CrossRef](#)]
25. Haralampous, O.; Dritselis, C. *Modeling of the Loading in Partially Damaged DPFs*; MODEGAT IV: Bad-Herrenalb, Germany, 2015.
26. Haralampous, O.; Mastellos, D. A multi-channel mathematical model for partially failed diesel particulate filters. In Proceedings of the 8th GRACM International Congress on Computational Mechanics, Volos, Greece, 12–15 July 2015.
27. Nield, D.A.; Bejan, A. *Convection in Porous Media*; Springer: New York, NY, USA, 1998.
28. Bhattacharyya, S.; Dinakaran, S.; Khalili, A. Fluid motion around and through a porous cylinder. *Chem. Eng. Sci.* **2006**, *61*, 4451–4461. [[CrossRef](#)]
29. Breugem, W.P.; Boersma, B.J.; Uittenbogaard, R.E. The influence of wall permeability on turbulent channel flow. *J. Fluid Mech.* **2006**, *562*, 35–72. [[CrossRef](#)]
30. Wu, H.; Wang, R. Convective heat transfer over a heated square porous cylinder in a channel. *Int. J. Heat Mass Trans.* **2010**, *53*, 1927–1937. [[CrossRef](#)]
31. Orlanski, I. A simple boundary condition for unbounded hyperbolic flows. *J. Comput. Phys.* **1976**, *21*, 251–269. [[CrossRef](#)]
32. Fu, W.; Huang, H.; Liou, W. Thermal enhancement in laminar channel flow with a porous block. *Int. J. Heat Mass Trans.* **1996**, *39*, 2165–2175. [[CrossRef](#)]
33. Bhattacharyya, S.; Singh, A.K. Augmentation of heat transfer from a solid cylinder wrapped with a porous layer. *Int. J. Heat Mass Tran.* **2009**, *52*, 1991–2001. [[CrossRef](#)]
34. Dhinakaran, S.; Ponmozhi, J. Heat transfer from a permeable square cylinder to a flowing fluid. *Energy Convers. Manag.* **2011**, *52*, 2170–2182. [[CrossRef](#)]
35. Patankar, S.V. *Numerical Heat Transfer and Fluid Flow*; Hemisphere Publishing Corporation, Taylor and Francis Group: New York, NY, USA, 1980.
36. Ochoa-Tapia, J.A.; Whitaker, S. Momentum transfer at the boundary between a porous medium and a homogeneous fluid—I. Theoretical development. *Int. J. Heat Mass Trans.* **1995**, *38*, 2635–2646. [[CrossRef](#)]
37. Rosti, M.E.; Cortelezzi, L.; Quadrio, M. Direct numerical simulation of turbulent channel flow over porous walls. *J. Fluid Mech.* **2015**, *784*, 396–442. [[CrossRef](#)]
38. Crowe, C.; Sommerfeld, M.; Tsuji, Y. *Multiphase Flows with Droplets and Particles*; CRC Press: Boca Raton, FL, USA, 1998.
39. Ounis, H.; Ahmadi, G.; McLaughlin, J.B. Brownian diffusion of submicrometer particles in the viscous sublayer. *J. Colloid Interface Sci.* **1991**, *147*, 266–277. [[CrossRef](#)]
40. Li, A.; Ahmadi, G. Deposition of aerosols on surfaces in a turbulent channel flow. *Int. J. Eng. Sci.* **1993**, *31*, 435–451. [[CrossRef](#)]
41. Clift, R.; Grace, J.R.; Weber, M.E. *Bubbles, Drops and Particles*; Academic: New York, NY, USA, 1978.
42. Dritselis, C.D.; Vlachos, N.S. Numerical investigation of momentum exchange between particles and coherent structures in low Re turbulent channel flow. *Phys. Fluids* **2011**, *23*, 025103:1–025103:15. [[CrossRef](#)]
43. Haralampous, O.; Mastrokalos, M.; Tzorbatzoglou, F.; Dritselis, C. Experimental and computational investigation of particle filtration in partially damaged DPFs. In *SAE Technical Paper 2019-24-149*; SAE: Warrendale, PA, USA, 2019.
44. Sharipov, F.; Seleznev, V. Data on internal rarefied gas flows. *J. Phys. Chem. Ref. Data* **1998**, *27*, 657–706. [[CrossRef](#)]
45. Dritselis, C.D. On the enhancement of particle deposition in turbulent channel airflow by a ribbed wall. *Adv. Powder Technol.* **2017**, *28*, 922–931. [[CrossRef](#)]
46. Dritselis, C.D. Numerical study of particle deposition in a turbulent channel flow with transverse roughness elements on one wall. *Int. J. Multiph. Flow* **2017**, *91*, 1–18. [[CrossRef](#)]
47. Costa, V.A.F.; Oliveira, L.A.; Baliga, B.R.; Sousa, A.C.M. Simulation of coupled flows in adjacent porous and open domains using a control-volume finite-element method. *Numer. Heat Transf. Part A* **2004**, *45*, 675–697. [[CrossRef](#)]
48. Gartling, D.K.; Hickox, C.E.; Givler, R.C. Simulation of coupled viscous and porous flow problems. *Comput. Fluid Dyn.* **1996**, *7*, 23–48. [[CrossRef](#)]

49. Gavrilakis, S. Numerical simulation of low Reynolds number turbulent flow through a straight square duct. *J. Fluid Mech.* **1992**, *244*, 101–112. [[CrossRef](#)]
50. Hinze, J.O. *Turbulence*; McGraw–Hill: New York, NY, USA, 1975.
51. Breuer, M.; Bernsdorf, J.; Zeiser, T.; Durst, F. Accurate computations of the laminar flow past a square cylinder based on two different methods: Lattice-Boltzmann and finite-volume. *Int. J. Heat Fluid Flow* **2000**, *21*, 186–196. [[CrossRef](#)]
52. Ström, H.; Sasic, S.; Andersson, B. Effect of the turbulent-to-laminar transition in monolithic reactors for automotive pollution control. *Ind. Eng. Chem. Res.* **2011**, *50*, 3194–3205. [[CrossRef](#)]
53. Cornejo, I.; Nikrityuk, P.; Hayes, R.E. Turbulence generation after a monolith in automotive catalytic converters. *Chem. Eng. Sci.* **2011**, *187*, 107–116. [[CrossRef](#)]
54. Liu, Y.; Gong, J.; Fu, J.; Cai, H.; Long, G. Nanoparticle motion trajectories and deposition in an inlet channel of wall-flow diesel particulate filter. *Aerosol Sci.* **2009**, *40*, 307–323. [[CrossRef](#)]



© 2019 by the authors. Licensee MDPI, Basel, Switzerland. This article is an open access article distributed under the terms and conditions of the Creative Commons Attribution (CC BY) license (<http://creativecommons.org/licenses/by/4.0/>).